













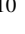

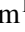
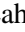




SN 2021adxl: A luminous nearby interacting supernova in an extremely low metallicity environment

S. J. Brennan¹ , S. Schulze^{2,3} , R. Lunnan¹ , J. Sollerman¹ , L. Yan⁴ , C. Fransson¹ , I. Irani⁵ , J. Melinder¹ , T.-W. Chen⁶ , K. De⁷ , C. Fremling⁴ , Y.-L. Kim⁸ , D. Perley⁹ , P. J. Pessi¹ , A. J. Drake¹⁰ , M. J. Graham¹⁰ , R. R. Laher¹¹ , F. J. Masci¹¹ , J. Purdum⁴ , and H. Rodriguez⁴ 

¹ The Oskar Klein Centre, Department of Astronomy, Stockholm University, AlbaNova, SE-10691 Stockholm, Sweden

² Center for Interdisciplinary Exploration and Research in Astrophysics (CIERA), Northwestern University, 1800 Sherman Ave., Evanston, IL 60201, USA

³ The Oskar Klein Centre, Department of Physics, Stockholm University, Albanova University Center, 106 91 Stockholm, Sweden

⁴ Caltech Optical Observatories, California Institute of Technology, Pasadena, CA 91125, USA

⁵ Department of Particle Physics and Astrophysics, Weizmann Institute of Science, 234 Herzl St, 7610001 Rehovot, Israel

⁶ Graduate Institute of Astronomy, National Central University, 300 Jhongda Road, 32001 Jhongli, Taiwan

⁷ MIT-Kavli Institute for Astrophysics and Space Research, 77 Massachusetts Ave., Cambridge, MA 02139, USA

⁸ Department of Physics, Lancaster University, Lancaster LA1 4YW, UK

⁹ Astrophysics Research Institute, Liverpool John Moores University, IC2, Liverpool Science Park, 146 Brownlow Hill, Liverpool L3 5RF, UK

¹⁰ Division of Physics, Mathematics and Astronomy, California Institute of Technology, Pasadena, CA 91125, USA

¹¹ IPAC, California Institute of Technology, 1200 E. California Blvd, Pasadena, CA 91125, USA

October 18, 2024

ABSTRACT

SN 2021adxl is a slowly evolving, luminous, Type II_n supernova with asymmetric emission line profiles, similar to the well-studied SN 2010jl. We present extensive optical, near-ultraviolet, and near-infrared photometry and spectroscopy covering ~ 1.5 years post discovery. SN 2021adxl occurred in an unusual environment, atop a vigorously star-forming region which is offset from its host galaxy core. The appearance of Ly α , O II, as well as the compact core, would classify the host of SN 2021adxl as a Blueberry galaxy, analogous to higher redshift, low metallicity, star-forming dwarf “Green Pea” galaxies. Using several abundance indicators, we find a metallicity of the explosion environment of only $\sim 0.1 Z_{\odot}$, the lowest reported metallicity for a Type II_n SN environment. SN 2021adxl reaches a peak magnitude of $M_r \approx -20.2$ mag and since discovery, SN 2021adxl has faded by only ~ 4 magnitudes in the r band with a cumulative radiated energy of $\sim 1.5 \times 10^{50}$ erg over 18 months. SN 2021adxl shows strong signs of interaction with a complex circumstellar medium, seen by the detection of X-rays, revealed by the detection of coronal emission lines, and through multi-component hydrogen and helium profiles. In order to further understand this interaction, we model the H α profile using a Monte-Carlo electron scattering code. The blueshifted high-velocity component is consistent with emission from a radially thin, spherical shell resulting in the broad emission components due to electron scattering. Using the velocity evolution of this emitting shell, we find that the SN ejecta collide with circumstellar material of at least $\sim 5 M_{\odot}$ assuming a steady-state mass-loss rate of $\sim 4 - 6 \times 10^{-3} M_{\odot} \text{ yr}^{-1}$ for the first ~ 200 days of evolution. SN 2021adxl was last observed to be slowly declining at $\sim 0.01 \text{ mag d}^{-1}$, and if this trend continues, SN 2021adxl will remain observable after its current solar conjunction. Continuing the observations of SN 2021adxl may reveal signatures of dust formation or an infrared excess, similar to that seen for SN 2010jl.

Key words. Supernovae: individual: SN 2021adxl – Supernovae: individual: SN 2010jl – Stars: winds, outflows

1. Introduction

Massive stars ($> 8 M_{\odot}$) are expected to end their lives as core-collapse supernovae (CCSNe) (Woosley & Weaver 1995; Heger et al. 2003; Janka 2012; Crowther 2012). All-sky photometric surveys (Bellm 2014; Chambers et al. 2016a; Tonry et al. 2018) are finding numerous supernovae (SNe) each night, but the exact mechanisms by which a massive star spends its final moments is currently unclear (see e.g., Burrows & Vartanyan 2021). Supernovae that display narrow Hydrogen emission lines atop a blue continuum are classified as Type II_n SNe (Schlegel 1990; Gal-Yam et al. 2007; Ransome et al. 2021). The narrow emission features are suggested to arise from the excitation of a slow-moving circum-stellar medium (CSM) near the progenitor which has been photoionised by the ejecta-CSM interaction.

This CSM is expected to have been ejected by the progenitor in the years to decades before core collapse (Vink et al. 2008; Ofek et al. 2014). While a star will eject mass into the surrounding interstellar medium (ISM) throughout its life, in the form of stellar winds with mass-loss rates of $10^{-7} - 10^{-4} M_{\odot} \text{ yr}^{-1}$, studies of the progenitors of Type II_n SNe have reported much higher mass-loss rates of $> 10^{-3} M_{\odot} \text{ yr}^{-1}$ (Fransson et al. 2014; Moriya et al. 2014; Fraser 2020; Khatami & Kasen 2023). This likely reflects either eruptive mass-loss events, or enhanced steady state mass loss by the progenitor in the decades prior to core-collapse.

The physical mechanism behind such an enhanced mass-loss rate is elusive, mainly due to the inability to directly observe these mass-loss events prior to the supernova explosion. However, this brief period of enhanced mass loss likely influences

the photometric evolution of the supernova, including duration and luminosity, as well as the spectroscopic appearance of emission/absorption line profiles and their evolution (for example see Kurfürst & Kr̄tička 2019; Suzuki et al. 2019, for the case of a disk/torus). These progenitors must have mass-loss rates not typically observed during the main sequence. It is suggested that the high mass-loss rates are similar to those of massive ($> 25 M_{\odot}$) luminous blue variable (LBV) stars (e.g. Taddia et al. 2013; Weis & Bomans 2020) and some Type II_n SNe have been associated with such stars (e.g. SN 2005gl; Gal-Yam et al. 2007). Alternatively, Type II_n SNe may arise as a result of a superwind phase from a red super-giant (RSG) star (Fransson et al. 2002; Smith et al. 2009a). Current stellar evolution theory suggests that canonical LBVs are a short transitional phase, between a hydrogen-rich RSG evolving towards a hydrogen-depleted Wolf-Rayet (WR) star (Crowther 2007; Langer 2012; Ekström et al. 2012). The term LBV is typically employed to define a broad phenomenology rather than an evolutionary stage (e.g. Gal-Yam et al. 2007; Trundle et al. 2008; Dwarkadas 2011; Groh 2017). Standard stellar evolution theory predicts that single massive stars which become LBVs do so near the end of, or after, the completion of core hydrogen burning. Thereafter they typically lose their hydrogen-rich envelopes in the LBV phase and become WR stars, where they spend $\sim 10^5$ years after which they explode as a CCSN.

To date, there is no clear understanding of how a star may undergo core-collapse at this phase (Chevalier 2012; Woosley 2017). However, under certain conditions, a progenitor may have the appearance of a LBV star shortly before core-collapse when the progenitor is rapidly rotating (e.g. Groh et al. 2013). In this scenario, the progenitor likely ejects the majority of its outer envelope during the RSG stage. It should be noted that these stars appear as LBV stars but do not necessarily have the chemical composition of the canonical LBV (Humphreys & Davidson 1994; Weis & Bomans 2020). Studies of Type II_n SNe show a diverse range of peak magnitudes, ranging from -16 to -23 magnitudes (Nyholm et al. 2020; Ransome et al. 2021). Typically, SNe brighter than -21 mag are classified as superluminous supernovae (SLSNe) (Gal-Yam 2012, 2019), although for hydrogen-rich transients it is not clear if there is a defined boundary between regular SNe and SLSNe (of Type II_n) or rather an apparent continuity.

This paper presents a large dataset for SN 2021adxl that enables us to study the late time evolution and environment of a nearby luminous Type II_n SN. A image of SN 2021adxl and its environment is given in Fig. 1. SN 2021adxl¹ was discovered by the Zwicky Transient Factory (ZTF; Graham et al. 2019; Bellm et al. 2019; Dekany et al. 2020) at R.A. = 11:48:06.940, DEC. = $-12:38:41.71$ (J2000) on 2021-11-08 at a r -band magnitude of 14.41 mag (Fremling 2021). SN 2021adxl was classified by De et al. 2022 on 2022-02-02 as a Type II_n SN at a redshift of $z = 0.018$ (reported wavelengths given in rest frame unless stated otherwise). The host of SN 2021adxl, WISEA J114806.88-123841.3, displays a unique morphology known in the literature as a Tadpole Galaxy (Elmegreen et al. 2012; Munoz-Tunon et al. 2014; Rosado-Belza et al. 2019), discussed further in Sec. 3. We assume a Hubble constant $H_0 = 73 \text{ km s}^{-1} \text{ Mpc}^{-1}$, $\Omega_{\Lambda} = 0.73$ and $\Omega_M = 0.27$ (Spergel et al. 2007). The corresponding luminosity distance $D_L = 78.16 \text{ Mpc}$ and a distance modulus of $\mu = 34.47 \pm 0.02 \text{ mag}$ are used for SN 2021adxl. We correct for foreground extinction using $R_V=3.1$, $E(B - V) = 0.026$ and the

¹ Also known as Gaia21fcd, PS22bne, ATLAS23blun, and ZTF21ackxdos.

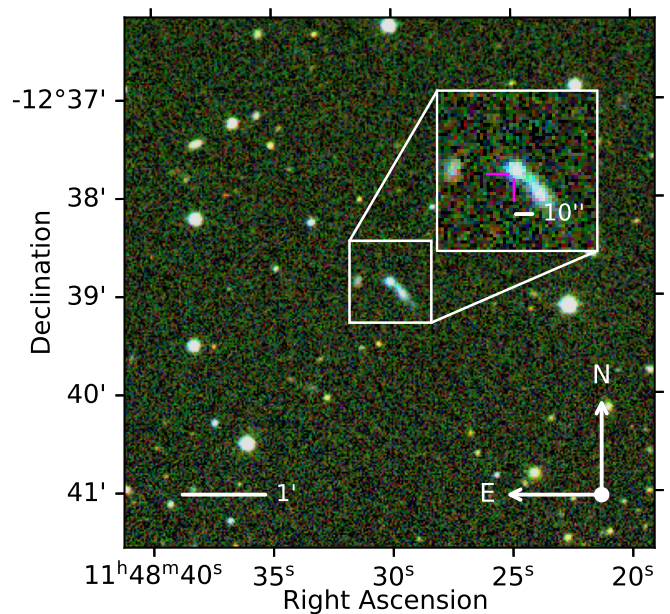


Fig. 1: P60/SEDM composite color image (gri) for SN 2021adxl (marked in the inset by the magenta crosshair) from the ZTF survey, when the transient was near peak. SN 2021adxl is situated atop strong host emission, which can be seen in the inset.

extinction law given by Cardelli et al. 1989. Unless stated, we do not correct for any potential host galaxy or circumstellar extinction, however we note that the blue colors seen in the spectra of SN 2021adxl, as well as the host, do not point towards significant reddening by dust. Additionally the lack of noticeable Na D $\lambda\lambda 5890$ 5896 points towards low extinction, although a robust measurement cannot be made to do the strong He I $\lambda 5876$ emission. The rising part of the light curve of SN 2021adxl was not observed, as the transient was discovered around its peak magnitude after ending solar conjunction. The rest-frame phase is taken with respect to the r -band discovery epoch on 2021-11-03 (MJD = 59521). Luminous SNe are intrinsically rare and given the adopted distance of 78 Mpc, SN 2021adxl is the nearby Type II_n SN, and just as SN 2010jl (49 Mpc; Smith et al. 2011; Fransson et al. 2014; Ofek et al. 2014; Jencson et al. 2016), and due to its luminosity and slow evolution, provides a rare opportunity to follow the evolution of such a transient for many years.

This paper is organised as follows: Section 2 provides details of the observational dataset presented in this paper, split into photometric in Sect. 2.1 and spectroscopic data in Sect. 2.2, as well as gives an overview of the observable properties for SN 2021adxl. SN 2021adxl occurred in a bright star forming region, and we discuss the host environment of SN 2021adxl in Sect. 3. A prominent feature of the optical spectra of SN 2021adxl is the broad H α profile, and we explore the formation of this line in Sect. 4, as well as any insight into the ejecta-CSM interaction in Sect. 4.1. Finally in Sect. 5, using the results from observations, we investigate the metallicity of the host of SN 2021adxl and, in general, interacting SNe in Sect. 5.2 as well as discuss the possible progenitor of SN 2021adxl in Sect. 5.3.

2. Observations

2.1. Photometry

Photometry in *gri* was obtained at the position of SN 2021adxl using the ZTF forced-photometry service² (Masci et al. 2019). Quality checks are performed on the raw data and detections are chosen based on a signal-to-noise ratio (S/N) of $S/N \geq 3$. Photometry from the ATLAS forced-photometry server³ (Tonry et al. 2018; Smith et al. 2020; Shingles et al. 2021) at the position of SN 2021adxl were obtained in the ATLAS *c* and *o* filters. We compute the weighted average of the fluxes of the observations on nightly cadence. We perform a quality cut of 3σ in the resulting flux of each night for both filters and then convert them to the AB magnitude system. A single epoch of photometry with the AAlhambra Faint Object Spectrograph and Camera, (ALFOSC) on the 2.56 m Nordic Optical Telescope (NOT) was obtained in *gr* and three epochs from the Liverpool Telescope (LT) with the optical imaging component of IO (Infrared-Optical) instrument was obtained in *gri*. J-band photometry was obtained with the Palomar Gattini-IR (PGIR) telescope shortly after SN 2021adxl was discovered and data were reduced following De et al. 2020. No significant activity/outbursts are detected in the pre-discovery images extending back to the beginning of the ZTF observing (circa 2018) to a limit of -14 mag. Our photometric dataset is given in Fig. 2 and photometric tables are available in the online material.

We observed the field SN 2021adxl with the Swift’s onboard X-ray telescope XRT (Burrows et al. 2005) in photon-counting mode between 2022-02-23T16:47:35 (MJD: 59633.699) and 2022-04-16T12:19:33 (MJD: 59685.5136). We analysed all photon-counting data with the online tools of the UK Swift team that use the methods described by Evans et al. 2007, 2009, 2020 and the software package HEASoft⁴.

An image constructed from all XRT data reveals a fading source at RA, Decl. (J2000) 11:48:06.72, -12:38:45.0 with an uncertainty of 5.3 arcsec (radius, 90% confidence), using the online tool of the UK Swift team⁵ (Evans et al. 2007, 2009). Using the dynamic binning method of the swift online tools, we obtain two detections summarised in Table 1. The number of counts is too low to robustly constrain the X-ray spectrum. To convert the count-rate to a flux, we assume an absorbed power-law with a photon index of 2 where the absorption components is set to the Milky-Way value of $N(\text{H}, \text{Gal}) = 2.74 \times 10^{20} \text{ cm}^{-2}$ from (HI4PI Collaboration et al. 2016). Using these spectral parameters, we derive count rate to flux conversion factor of $3.75 \times 10^{-11} \text{ erg s}^{-1} \text{ cm}^{-2} / (\text{ct s}^{-1})$ to infer the unabsorbed flux between 0.3 and 10 keV. The converted count rates are summarised in Table 1, and we will further discuss the X-ray luminosity in Sect. 2.5.

Due to its proximity at only 78 Mpc, and the fact that SN 2021adxl is a slow evolving luminous transient, fading by only 4.5 mags during the 1.5 year (18 month) dataset presented in this work, this SN can potentially be followed-up for years. Figure 2 illustrates the entire multi-band observations of SN 2021adxl covering from discovery until solar conjunction in mid-2023. Spectroscopic follow-up began in February 2021, and is discussed further in Sect. 2.2.

The lightcurve of SN 2021adxl shows two distinct phases (referred to as Phase 1 and Phase 2) in its post-peak evolution.

Table 1: Log of XRT observations

MJD	Phase (days)	Count rate (10^{-3} s^{-1})	F (0.3 – 10 keV) ($10^{-12} \text{ erg s}^{-1} \text{ cm}^{-2}$)
59633.9 ^{+26.1} _{-0.2}	+113	0.011 ± 0.003	0.41 ± 0.10
59681.4 ^{+4.3} _{-13.5}	+161	0.003 ± 0.001	0.12 ± 0.05

Notes. The flux reports the brightness after accounting for absorption in the Milky Way.

The peak itself is poorly sampled and it is unclear if Phase 1 extends to the earliest detections. Approximately 100 days post discovery, SN 2021adxl shows smooth decline of $\sim 0.6 \text{ mag} / 100 \text{ d}$, declining faster in the bluer bands, as is typical for Type II_n SNe (see Fig. 10 in Nyholm et al. 2020). After the mid-2022 solar conjunction, SN 2021adxl begins to decline at a slightly faster rate of $1 \text{ mag} / 100 \text{ d}$.

The rise to peak for SN 2021adxl was not observed due to solar conjunction in late-2021. An important aspect of Type II_n SNe is their rise time to maximum light, as there is a strong correlation between rise time and CSM/ejecta properties (e.g. Suzuki et al. 2016; Nyholm et al. 2020). The inset of Fig. 2 shows the Gaia G-band observations of the site of SN 2021adxl covering the past 9 years. Prior to SN 2021adxl, there is no significant variability seen at the explosion site. Similarity, no precursor signal is seen in forced-photometry measurements of ZTF, and ATLAS observations.

A pseudo-bolometric lightcurve is constructed using SUPERBOL⁶ (Nicholl 2018) from the photometry presented in Fig. 2, and calibrated using the extinction and distance given in Sect. 1. The resulting lightcurve is shown in Fig. 5. The bolometric light curve can be accurately characterized by a power law decay from $\sim 0 - 300$ days (with respect to discovery date), given by $L \approx 7.81 \times 10^{42} \times (t/100 \text{ days})^{-1.13} \text{ erg s}^{-1}$ and a final steep decay given as $L \approx 2.17 \times 10^{42} \times (t/300 \text{ days})^{-3.89} \text{ erg s}^{-1}$ after ~ 300 days. As shown in Fig. 5, this is similar to SN 2010jl (Fransson et al. 2014), but SN 2021adxl is around 66% less luminous.

Figure 3 compares the *r/R*-band absolute light curve of SN 2021adxl with several transients with similar photometric appearance, most notably SN 2013L (Andrews et al. 2017; Taddia et al. 2020) and SN 2010jl (Fransson et al. 2014; Jencson et al. 2016). Additionally, Fig. 4 gives the extinction-corrected color evolution for each transient. Qualitatively, SN 2021adxl, SN 2013L, and SN 2010jl share the same lightcurve morphology and color evolution. Post-peak, each of these transients light curves flattens after ~ 100 days. SN 2021adxl shows a steeper decline compared to SN 2013L and SN 2010jl, with a slope similar to that seen in SN 2016aps (Nicholl et al. 2020), albeit ~ 2 mags less luminous.

After ~ 250 days, SN 2021adxl begins to decline faster, and the same evolution is also clearly seen for SN 2010jl and SN 2013L, although with much poorer cadence for the latter. A similar trend was observed also for the Type II_n SN 2005ip, however for that SN the first flattening stage happened later, at approximately +200 days (Stritzinger et al. 2012) and the second drop-off much later, at +3000 days (Fox et al. 2020). For contrast, the prototype Type II_n SN 1998S does not show any light-curve flattening, but declines rather quickly (Schlegel 1990; Mauerhan & Smith 2012).

As seen from Fig. 3, there is a spread in peak magnitudes for the transients. Under the assumption that the explosion mecha-

⁶ <https://github.com/mnicholl/superbol>

² <https://ztfweb.ipac.caltech.edu/cgi-bin/requestForcedPhotometry.cgi>

³ <https://fallingstar-data.com/forcedphot/>

⁴ <https://heasarc.gsfc.nasa.gov/lheasoft>

⁵ http://www.swift.ac.uk/user_objects/

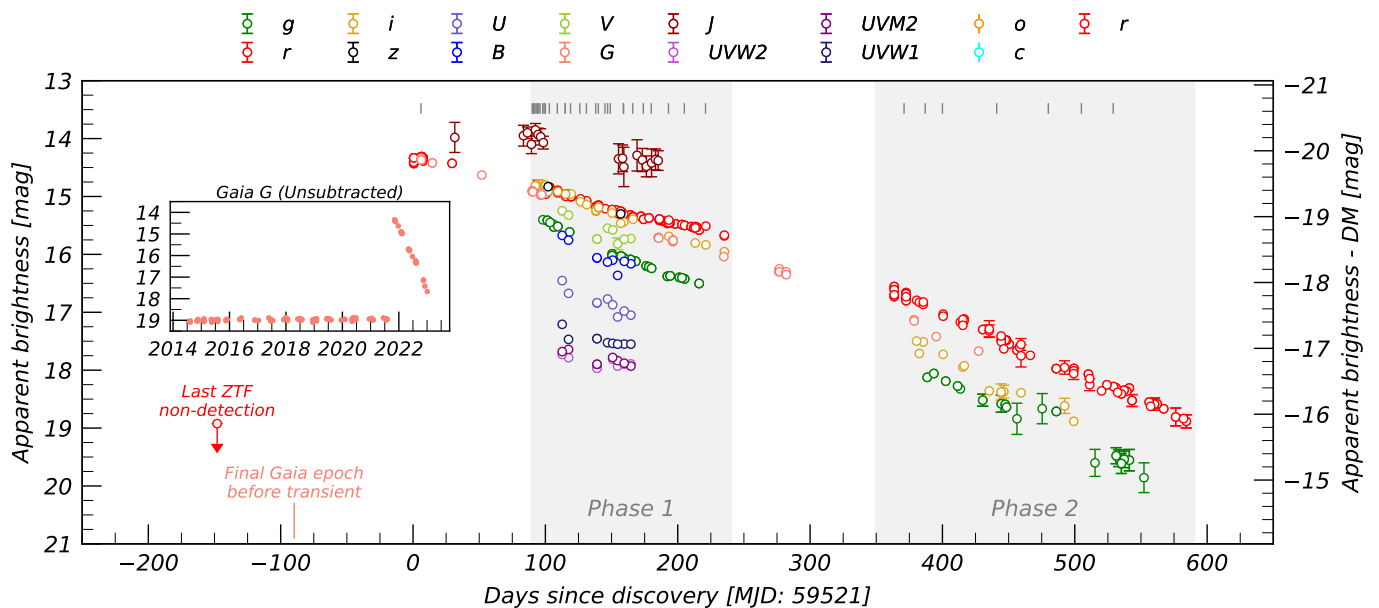


Fig. 2: Multi-band lightcurve of SN 2021adxl covering ~ 1.6 years of its post-peak evolution. Highlighted in grey are two distinct phases where SN 2021adxl displays two distinct decline slopes, as mentioned in the text. The inset provides Gaia G-band data of SN 2021adxl (post-2022), as well as the historic observations of the explosion site (pre-2022, likely dominated by host flux). The right y-axis gives the apparent magnitude corrected for distance. Spectral epochs are given as vertical lines at the top of the plot.

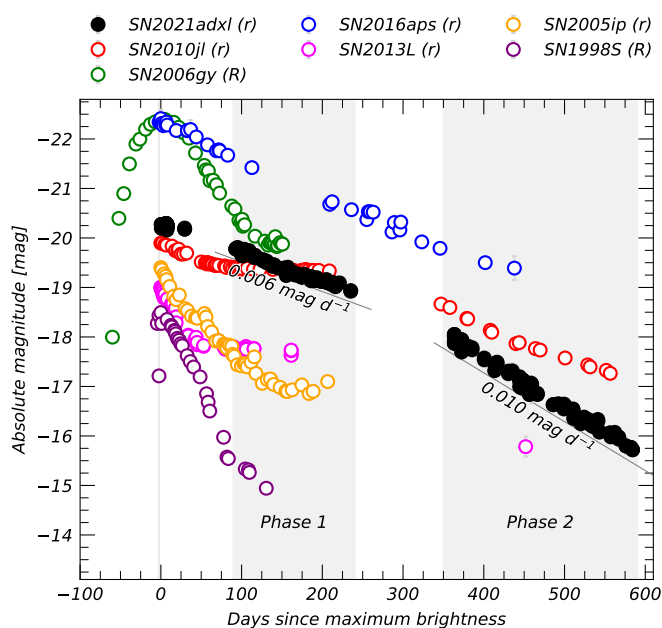


Fig. 3: r/R -band lightcurve comparison of luminous interacting SNe including SN 2021adxl. Each transient is corrected for distance and MW extinction. The regions marked as Phase 1 and Phase 2 correspond to the phases in the post-peak evolution where SN 2021adxl shows unique decline rates.

nism for each transient is similar, e.g. core-collapse (Bethe 1990; Woosley & Weaver 1995; Smartt 2009) or pulsational-pair instabilities (Woosley 2017), the heterogeneity in brightness could be the result of different amounts of CSM and/or ejecta mass, although this assumes the explosion energy is similar for all

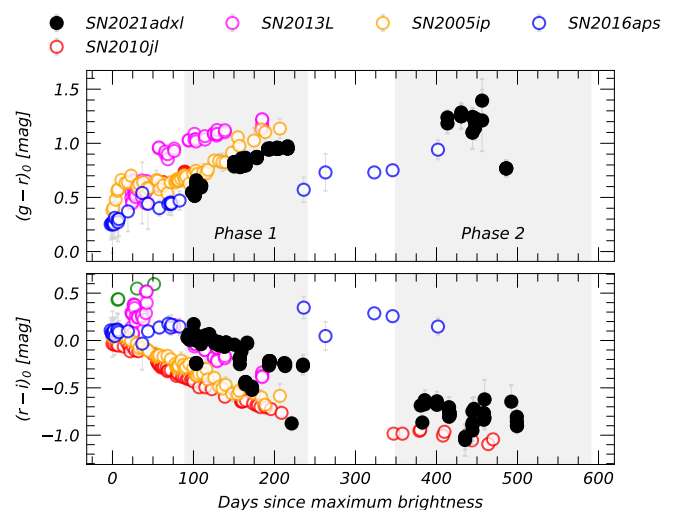


Fig. 4: Color comparison of bright Type IIIn SNe including SN 2021adxl. Each transient has been corrected for MW extinction.

Type IIIns. We further discuss the ejecta and CSM properties of SN 2021adxl in Sect. 4.1

2.2. Spectral evolution

Figure 6 shows the earliest spectrum of SN 2021adxl, taken around the (apparent) peak brightness. Although the spectrum shows some undulations, its overall appearance is consistent with a Type IIIn SN, i.e. a blue continuum with narrow Hydrogen emission features, with underlying host flux seen in [O III] $\lambda 5007$. SN 2021adxl was then classified as a Type IIIn by

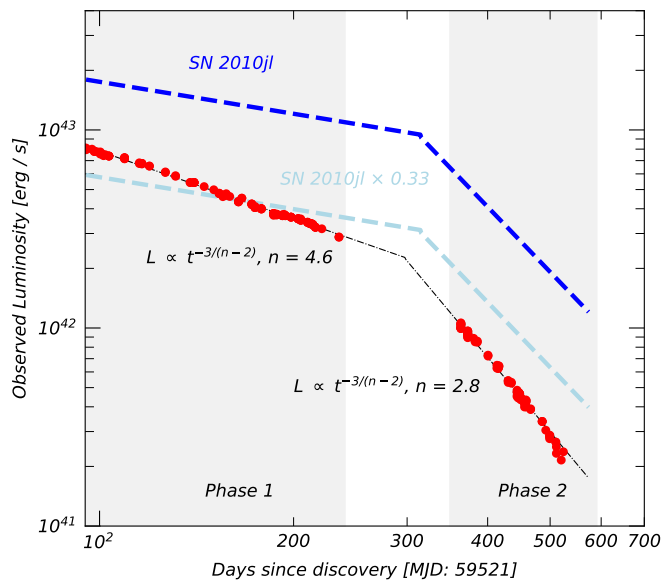


Fig. 5: Bolometric light curve for SN 2021adxl. The black dashed lines show power law fits to the phase 1 and phase 2 light curve, which a distinct break at $\sim +300$ days post discovery. The blue dashed line is the similar power law fits for SN 2010jl (Fransson et al. 2014), as well as the same fit scaled to match SN 2021adxl by eye in light blue.

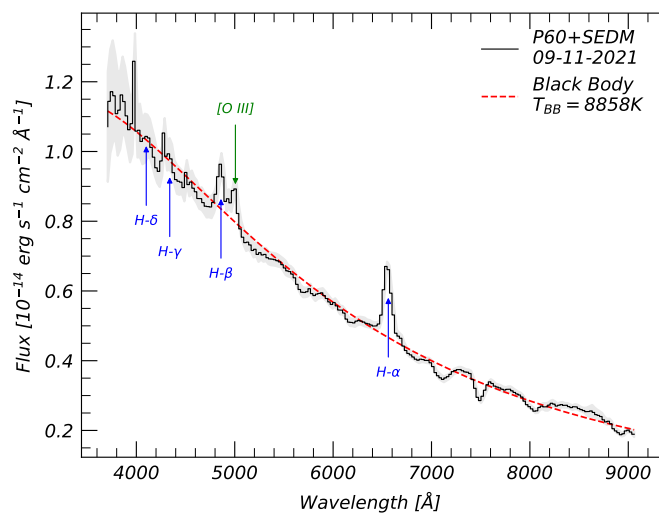


Fig. 6: The earliest spectrum of SN 2021adxl from P60/SEDMD taken on 2021-11-09. The mean flux is given in black, with 1σ errors shaded in grey.

De et al. 2022 using the Magellan/Baade with the FIRE NIR instrument on 2022-02-01 and the classification spectrum is shown in Fig. 7.

Follow-up spectra were obtained using NOT+ALFOSC, the Low Resolution Imaging Spectrometer (LRIS; Oke et al. 1995) on the 10 m Keck telescope, the Double Spectrograph (DBSP) on the Palomar 200-inch telescope (P200), and the Spectral Energy Distribution Machine (SEDMD; Blagorodnova et al. 2018; Rigault et al. 2019) on the Palomar 60-inch (P60) telescope. Observations using the P60 and P200 were coordinated using the FRITZ data platform (van der Walt et al. 2019; Coughlin et al.

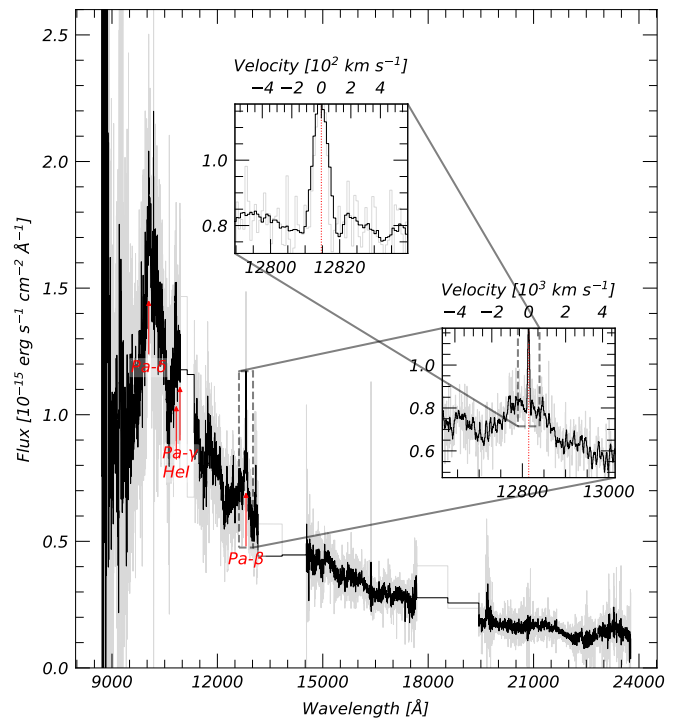


Fig. 7: Classification NIR spectrum of SN 2021adxl from the Magellan/FIRE from 2022-02-01 (De et al. 2022). A close-up of the Pa- β line is given in the inset on the right, with a zoomed-in profile in the upper left. The spectrum smoothed with a Savgol filter is given in black, with the raw data given in grey.

2023). The spectra were reduced in a standard manner, using LPIPE (Perley 2019), DBSP_DRP (Mandigo-Stoba et al. 2022) and PYPEIT (Prochaska et al. 2020a,b; Prochaska et al. 2020), for Keck/LRIS, P200/DBSP, and NOT/ALFOSC, respectively, and SEDMD spectra were reduced using the automated pipeline PYSEDM (Rigault et al. 2019; Kim et al. 2022).

A single UV spectrum was obtained using the Cosmic Origins Spectrograph (COS) onboard the Hubble Space Telescope (HST) on 2022-04-11 (Program ID: 16931, PI: Yan) and is presented in Fig. 8. This spectrum is low S/N (upper panel of Fig. 8), however when a smoothing filter is applied, we recover interstellar absorption bands (see Haser et al. 1998, and references therein), and several emission lines at the redshift of SN 2021adxl. Most features seen in the lower panel of Fig. 8 likely arise due to interstellar absorption within the MW, although we make tentative detections of N IV], O III], and He II, as well as Ly α , at the redshift of SN 2021adxl.

A near UV spectrum was obtained on 2022-04-11 (Program ID: 16931, PI: Yan) using the Space Telescope Imaging Spectrograph (STIS) aboard HST and is presented in Fig. 9. The spectrum's appearance does show some continuum flux, likely from SN 2021adxl, with a single broad feature at $\sim 2758\text{\AA}$. While this may be broad/blended Mg II $\lambda\lambda 2796, 2803$ (albeit offset by $F \sim 40\text{\AA}$), it is also possible a blend of several host/transient lines with superimposed interstellar lines, see inset of Fig. 9. The UV appearance of SN 2021adxl and its host is further discussed in Sect. 5.1.

We obtained four medium-resolution spectra with the X-shooter instrument (Vernet et al. 2011) between 2022-02-26 and 2023-02-26 (observing program 108.2262; PI: R. Lunnan). All observations were performed in nodding mode and with $1''/0$ /

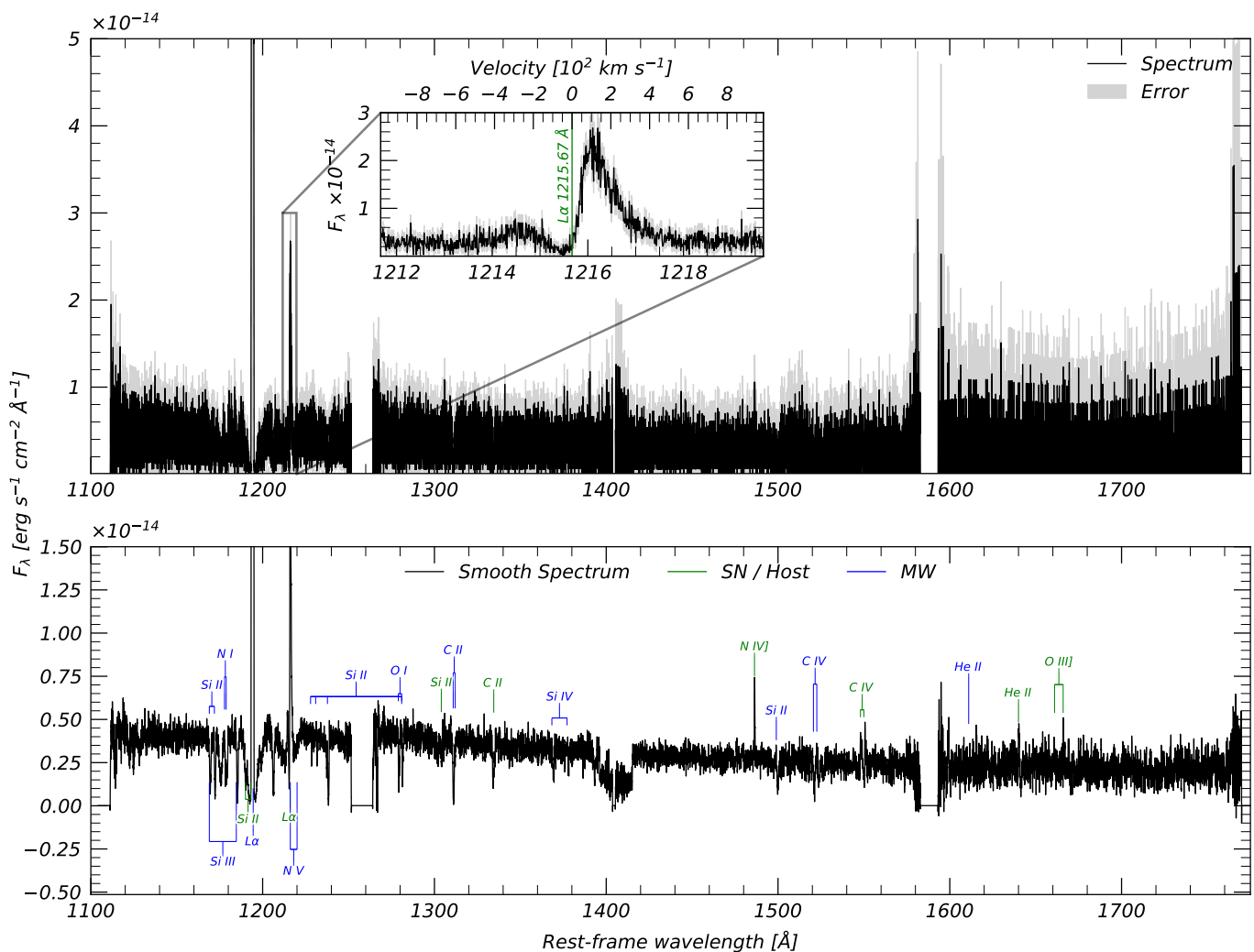


Fig. 8: HST/COS UV spectrum of SN 2021adxl taken with the G130M (FUV) and G160M (NUV) grism on 2022-04-11 (+158d). Upper panel shows the (error) spectrum given in (grey) black. Lower panel gives the science spectrum smoothed using a Savitzky–Golay (Savgol) filter with window size equal to 31 with a 2nd order polynomial. We include expected wavelengths for both Milky Way (MW) (blue) and SN 2021adxl plus its host (Green), although the detection of some of these lines are unclear due to the low S/N of the science spectrum.

0'9 / 0'9 wide slits (UVB / VIS / NIR). The first four epochs covered the full spectral range from 3000 to 24,800 Å. The integration times were varied between 2400 and 3700s. The data were reduced following Selsing et al. 2019. In brief, we first removed cosmic-rays with the tool `ASTROCRAPPY`⁷, which is based on the cosmic-ray removal algorithm by van Dokkum 2001. Afterwards, the data were processed with the X-shooter pipeline v3.3.5 and the ESO workflow engine ESOReflex (Goldoni et al. 2006; Modigliani et al. 2010). The UVB and VIS-arm data were reduced in stare mode to boost the S/N. In the background limited case, this can increase the S/N by a factor of $\sqrt{2}$ compared to the standard nodding mode reduction (in the background limited case). The individual rectified, wavelength- and flux-calibrated two-dimensional spectra files were co-added using tools developed by J. Selsing⁸. The NIR data were reduced in nodding mode to ensure a good sky-line subtraction. In the third step, we extracted the one-dimensional spectra of each arm in a statistically

optimal way using tools by J. Selsing. Finally, the wavelength calibration of all spectra were corrected for barycentric motion. The spectra of the individual arms were stitched by averaging the overlap regions. Note, to study the host galaxy, we reduced the data in nodding mode.

Figure 10 presents four epochs of spectroscopy taken with the VLT and the X-shooter medium resolution spectrograph. All spectra was observed at parallactic angle with the UV, optical and IR regions stitched using a chi-2 minimization and flux calibrated top photometry taken on the same night. Two spectra were obtained during Phase 1 of the lightcurve, and two during Phase 2. The spectra show contributions from both transient light, seen by the broader emission profiles, as well as flux from the underlying host. At the time of writing, SN 2021adxl still dominates the flux at the location, and templates are currently unobtainable in order to remove narrow emission components from the host. A log of the available spectra is provided in Table 2 and the epochs of spectroscopy are indicated in Fig. 2 as the vertical lines. All wavelength reports are given in rest-frame unless otherwise stated.

⁷ <https://github.com/astrophy/astrocrappy>

⁸ https://github.com/jselsing/XSGRB_reduction_scripts

Table 2: Spectroscopy log for SN 2021adxl. Phase with reference to discovery date [MJD 59521]

Date	MJD	Phase (d)	Telescope	Instrument	Resolution ($\lambda/\Delta\lambda$)	Exposure Time (s)
2021-11-09	59527	+6	P60	SEDM IFU	100	2400
2022-02-02	59612	+91	P200	DBSP	4000	300
2022-02-03	59613	+92	P60	SEDM IFU	100	2400
2022-02-04	59614	+93	P60	SEDM IFU	100	2400
2022-02-05	59615	+94	Keck	LRIS	300-5000	2400
2022-02-05	59615	+94	P60	SEDM IFU	100	2400
2022-02-06	59616	+95	P60	SEDM IFU	100	2400
2022-02-07	59617	+96	P60	SEDM IFU	100	2400
2022-02-09	59619	+98	P60	SEDM IFU	100	2400
2022-02-10	59620	+99	P60	SEDM IFU	100	2400
2022-02-11	59621	+100	P60	SEDM IFU	100	2400
2022-02-14	59624	+103	NOT	ALFOSC+Grism4	360	1800
2022-02-20	59630	+109	P60	SEDM IFU	100	2400
2022-02-26	59636	+115	VLT	X-shooter	5400/8900/5600	2400/2458/2400
2022-02-26	59636	+115	P60	SEDM IFU	100	2400
2022-03-02	59640	+119	P60	SEDM IFU	100	2160
2022-03-09	59647	+126	P60	SEDM IFU	100	2400
2022-03-14	59652	+131	P60	SEDM IFU	100	2400
2022-03-21	59659	+138	P60	SEDM IFU	100	2400
2022-03-21	59659	+138	P60	SEDM IFU	100	2400
2022-03-23	59661	+140	P60	SEDM IFU	100	2400
2022-03-23	59661	+140	P60	SEDM IFU	100	2400
2022-03-28	59666	+145	P60	SEDM IFU	100	2400
2022-03-30	59668	+147	NOT	ALFOSC+Grism4	360	1800
2022-04-01	59670	+149	P60	SEDM IFU	100	2400
2022-04-11	59680	+159	HST	COS/STIS	2000-3000	1911
2022-04-11	59680	+159	P60	SEDM IFU	100	2400
2022-04-18	59687	+166	P60	SEDM IFU	100	2160
2022-04-26	59695	+174	NOT	ALFOSC+ Grism4	360	1800
2022-05-02	59701	+180	VLT	X-shooter	5400/8900/5600	3600
2022-05-15	59714	+193	P60	SEDM IFU	100	2160
2022-05-27	59726	+205	NOT	ALFOSC+Grism4	360	1800
2022-06-12	59742	+221	P60	SEDM IFU	100	2160
2022-11-09	59892	+371	P60	SEDM IFU	100	2400
2022-11-25	59908	+387	NOT	ALFOSC+Grism4	360	1200
2022-12-08	59921	+400	P60	SEDM IFU	100	1800
2023-01-18	59962	+441	VLT	X-shooter	5400/8900/5600	1800/1860/1800
2023-02-26	60001	+480	VLT	X-shooter	5400/8900/5600	3600/3716/3600
2023-03-23	60026	+505	NOT	ALFOSC+Grism4	360	3300
2023-04-16	60050	+529	NOT	ALFOSC+Grism4	360	3300

2.3. Hydrogen spectral evolution

The most prominent and informative features in the spectra of Type II_n SNe is the Balmer series, and specifically the H α profile (e.g. Roming et al. 2012; Ransome et al. 2021; Pursiainen et al. 2022). The H α emission line has been used to constrain the progenitor wind velocity (Kankare et al. 2012; Andrews et al. 2017; Chugai 2019), explosion geometry (Hoffman et al. 2008; Andrews & Smith 2018; Pursiainen et al. 2022), and can potentially indicate late-time interaction (Silverman et al. 2013; Yan et al. 2015).

Type II_n SNe typically develop some asymmetries in their H α emission line profiles in the post peak evolution (Trundle et al. 2009; Fransson et al. 2014; Andrews et al. 2017, 2019; Moriya et al. 2020; Taddia et al. 2020; Pursiainen et al. 2022), and there are also cases where multiple absorption troughs are observed (Gutiérrez et al. 2017; Brennan et al. 2022). As noticed by De et al. (2022), the NIR classification spectrum for SN 2021adxl shows strong signs of hydrogen and helium emis-

sion. The insets of Fig. 7 give a close-up view of the Pa- β line, which is the best isolated hydrogen emission feature. In agreement with the initial classification, we resolve two apparent absorption features for the Pa- β line, one with a trough centered around ~ 3500 km s $^{-1}$ (right inset) and the second at ~ 200 km s $^{-1}$ (upper left inset). Although the latter has low S/N, a consistent absorption feature is seen also in other Paschen lines.

We observe a P-Cygni profile at the approximate wavelength of Ly α in Fig. 8. The emission of Ly α is redshifted by ~ 100 km s $^{-1}$, with a blueshifted absorption centered at ~ -100 km s $^{-1}$ (with respect to rest wavelength). Although the appearance of Ly α for SN 2021adxl is in contrast to the profile seen for SN 2010jl (Fransson et al. 2014), with SN 2021adxl showing a P-Cygni profile, and SN 2010jl showing a purely absorption profile. This redshifted profile for SN 2021adxl may be a result of electron scattering (Huang & Chevalier 2018). As this spectrum is obtained ~ 5 months post discovery, the P-Cygni absorption likely originates from the pre-supernova stellar wind, located at

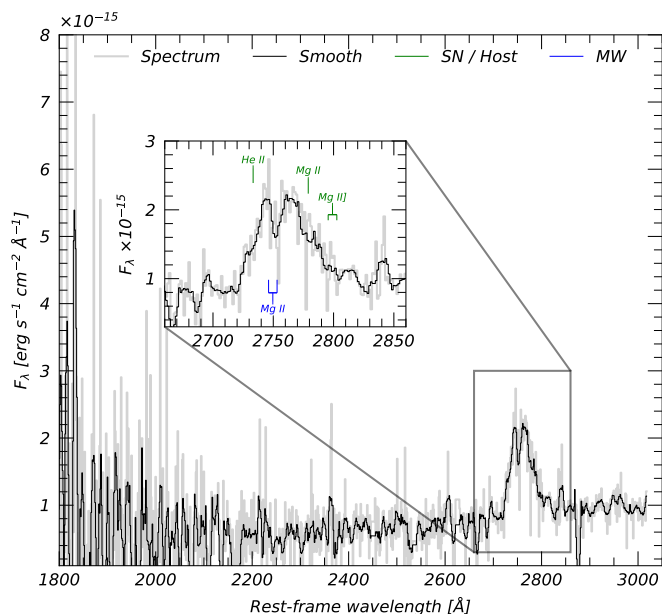


Fig. 9: HST/STIS with the G230LB grism on 2022-04-11 (+158d). The original science spectrum (grey) has been smoothed (black) using a Savgol filter with window size equal to 11 with a 2nd order polynomial. In the inset we show a close up of the broad feature around 2759Å and include expected wavelengths for both interstellar (blue) and SN 2021adxl (green) lines.

large distances from the ejecta-CSM interface. This is consistent with the absorption seen earlier in Fig. 7. This would also suggest that SN 2021adxl has a very extended, dense circumstellar environment, which is likely correlated with the slow evolution observed in Fig. 2. However, we can speculate that the strange Ly α emission profile is a result of the host environment itself. We discuss this further in Sect. 3

Figure 11 highlights the evolution of the H α profile from the VLT/X-shooter observations. The H α profile consists of multiple distinct components, giving rise to an overall asymmetric appearance. A prominent blue-shifted emission component is observed in H α and in other Balmer lines. This feature is not obviously seen in other emission features, for example in He I or Fe II, which suggests that the physical parameters forming this component are unique to a hydrogen-rich shell of material. This broad component does not extend to redder wavelengths, but the rather smooth line wings are indicative of electron scattering (Huang & Chevalier 2018). From the earliest X-shooter spectra, a third broad component can be resolved around rest wavelength with a superimposed narrow emission line likely arising from slow-moving CSM, an underlying H II region, or a combination of both.

As SN 2021adxl evolves, we see a smooth evolution of the H α profile, most notably of the blueward component. The upper panel of Fig. 12 shows the complete optical spectral dataset (excluding the low-resolution P60+SEDM spectra). We mark the point where the flux of H α exceeds 10% of the pseudo-continuum with a red cross. This component shows a smooth evolution during Phase 1, see lower panel of Fig. 12. During Phase 2 it is unclear if the H α velocity continues to follow this trend as it apparently shows a quicker decline in velocity.

Compared to photometrically similar objects, SN 2021adxl shows qualitative similarities to the Type II n SNe 2010jl (Fransson et al. 2014), 2013L (Andrews et al. 2017; Taddia et al. 2020) as well as SN 2005ip (Fox et al. 2020). Figure 13 compares the H α profile of SN 2021adxl, SN 2010jl, and SN 2013L. Each transient shows a smooth redward wing, likely a result of electron scattering, as well as a blueward excess that evolves with time. It should be noted that while these three transients are qualitatively similar photometrically and spectroscopically, the photometric decline times and the emission line amplitude and offset are different among these events, and this may be due to differences in mass, velocity, and distribution of the emitting material. This might also be reflected in the different lightcurves, see Fig. 3. Insights can be gained by noting the +115d spectrum of SN 2021adxl compared to a spectrum of SN 2010jl at a similar epoch (+94d). SN 2021adxl shows flux out to 8000 km s⁻¹ while SN 2010jl only shows a slight blue excess out to 2000 km s⁻¹, however this excess lines up quite well with the central wavelengths of the H α profile at this time. Whereas the H α profile of SN 2013L at this time matches the red wing of SN 2021adxl very well, and shows a much more dramatic flat-topped blue excess that persists for almost 4 years post peak (Andrews et al. 2017). Comparing the photometric evolution, SN 2013L shows a rapid decline before flattening, whereas SN 2010jl is more similar to SN 2021adxl, albeit declining at a slower rate.

2.4. Helium spectral evolution

Aside from hydrogen, the spectrum of SN 2021adxl is dominated by strong Helium emission features, such as He I λ 4471, λ 5876, λ 7065 and λ 10830, and possibly He I λ 2773 (see Fig. 9). In stark contrast to the H α line, the profile of He I λ 5876 resembles a P-Cygni profile. Figure 14 provides a cut-out around He I λ 5876, highlighting the strange P-Cygni-like profile with an absorption feature at \sim 4000 km s⁻¹.

Rather than the typical single absorption (e.g. Israelian & de Groot 1999), He I λ 5876 might show a second high velocity (HV) feature, extending out to \sim 18000 km s⁻¹. It is unclear whether this HV absorption is indeed associated with He I or a feature at bluer wavelength e.g. the Na I D doublet λ 5890, 5896, which is blended with the He I λ 5876 line. If this is the case, a large amount of sodium-rich material must remain optically thick more than 500 days post peak, and continue moving at very high velocities. In comparison to SN 2010jl, this double troughed absorption profile is not immediately obvious. In particular, the He I λ 5876 observed for SN 2010jl resembles the H α profile e.g. see Fig. 2.5

An alternative suggestion is that this HV material is associated with the He I λ 5876 line, although this feature is not clearly observed in other He I lines, due to severe line blending and/or tellurics bands, see Fig. 10. Seeing both absorption components would require an asymmetric explosion/CSM in order to see both the low and high velocity component, although maintaining a P-Cygni-like absorption profile after 500 days is also difficult to explain.

2.5. X-ray emission from Interacting SNe

When the progenitor of SN 2021adxl exploded, a shock wave was formed due to the collision of the fast moving ejecta and the slower moving CSM. X-ray emission, if detected, can be used to diagnose the shock wave interaction with the circumstellar medium (Chevalier & Fransson 2003; Dwarkadas 2019). We re-

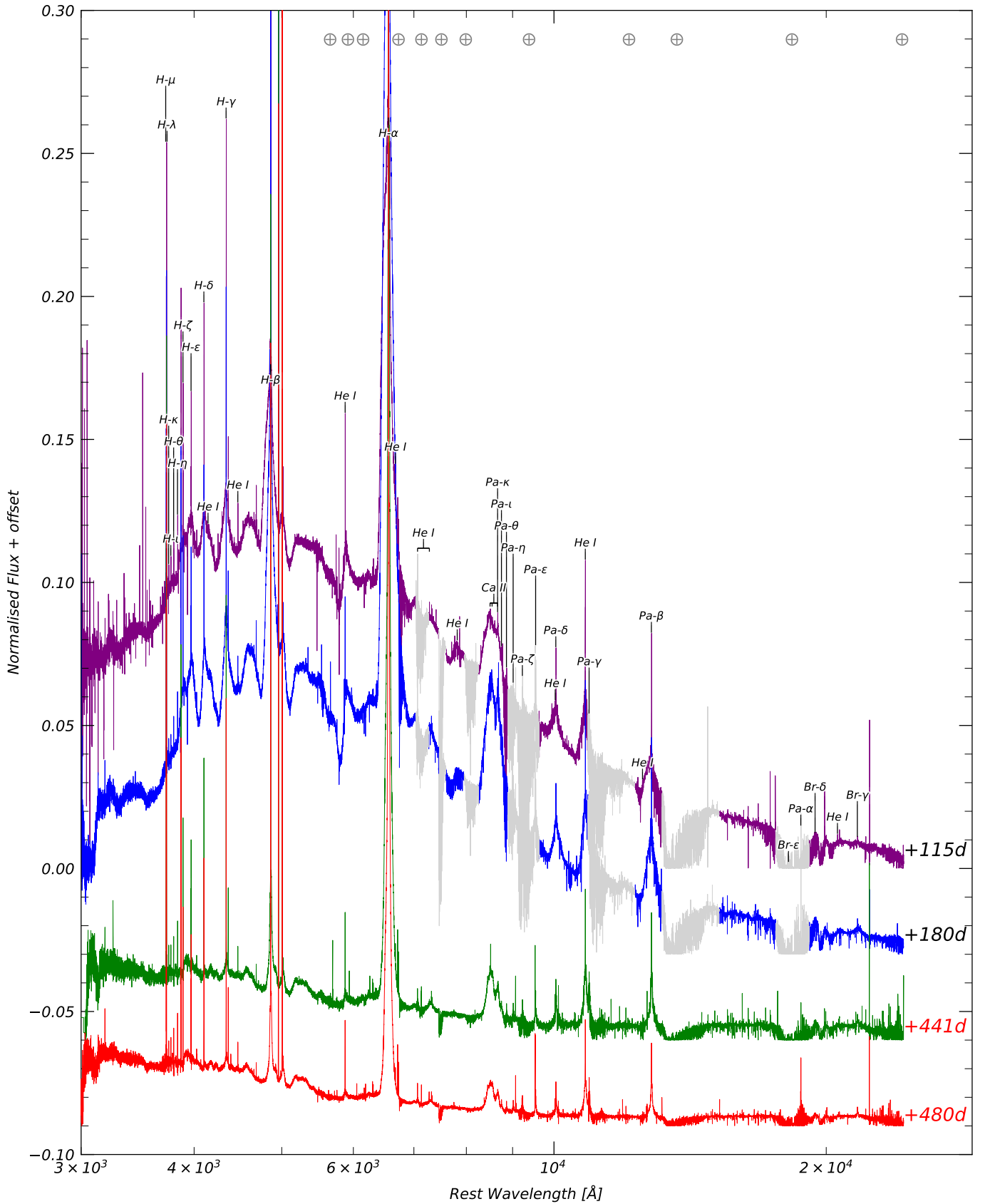


Fig. 10: VLT + X-shooter for SN 2021adxl taken at four different epochs. Each spectrum has been normalised with respect to H α and offset for clarity. Emission lines expected from the transient (black) are denoted by the vertical lines. Telluric absorption bands arising from atmospheric O₂ and H₂O are denoted by the \oplus symbol. We shaded in regions of high noise levels from our first two spectra for visual clarity.

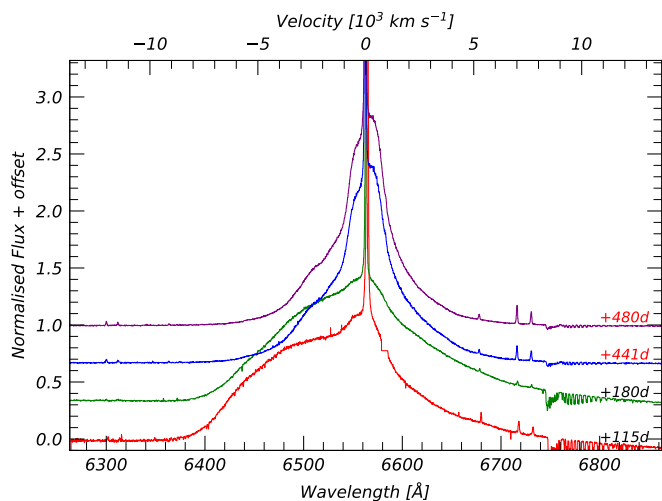


Fig. 11: Evolution of the $H\alpha$ profile from the VLT/X-shooter observations. A pseudo-continuum has been removed from each profile, and the spectra are normalised and offset for clarity. Phase given in grey (red) represents spectra obtained during (after) Phase 1. A noise spike at 6852\AA was manually removed from the +115 d spectrum.

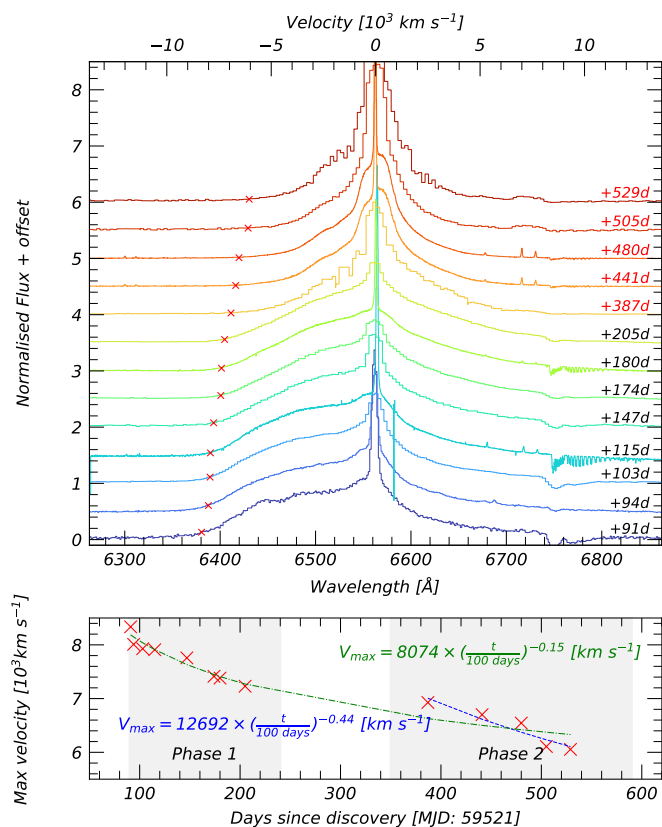


Fig. 12: Same as Fig. 11 but including the complete optical spectral dataset (excluding those from the P60/SEDM). A red cross on each profile denotes the maximum velocity of the blue excess for each spectrum. The lower panel gives the velocity of the bluest edge of the $H\alpha$ profile, marked by the red cross in the upper panel.

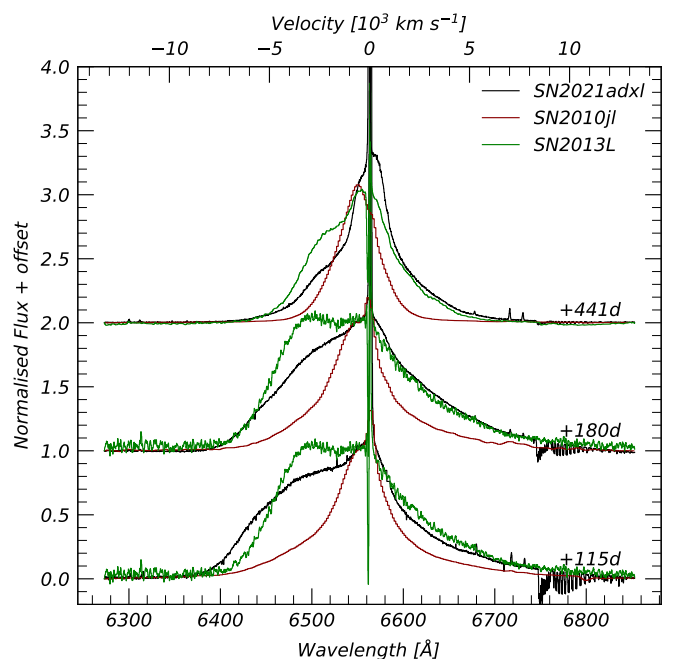


Fig. 13: Comparison of the $H\alpha$ profile from SN 2021adxl, SN 2010jl (Fransson et al. 2014), and SN 2013L (Andrews et al. 2017; Taddia et al. 2020). Each transient shows a blue shoulder atop their respective $H\alpha$ profile, as well as broad wings. Each profile has been normalised and offset for clarity.

ported the detection of a decaying X-ray flux at the position of SN 2021adxl (see Table. 1). This evolving X-ray is likely associated with SN 2021adxl and not the underlying source itself. We find the soft X-ray flux decreases from $\sim 3 \times 10^{40}$ ergs s^{-1} at +113d to $\sim 0.9 \times 10^{40}$ ergs s^{-1} at +160d. This flux is roughly a factor of 10 less than SN 2010jl (Chandra et al. 2015). However, meaningful comparison is moot due to the restricted X-ray cadence.

High ionization lines have been observed the optical spectra of nearby active galactic nuclei (AGNs) (Oke & Sargent 1968; Appenzeller & Oestreich 1988; Lamperti et al. 2017), however they are rarely observed in SNe (Turatto et al. 1993; Smith et al. 2009a), likely due to the lack of high to medium resolution spectra (Grönningsson et al. 2006; Komossa et al. 2009; Smith et al. 2009b; Pastorello et al. 2015; Fransson et al. 2014). These so-called “coronal lines”, first observed in the solar corona, arise from collisionally excited forbidden fine-structure transitions in highly ionized species such as Fe VI and Fe x.

Figure 15 shows our final X-shooter spectrum taken on 2023-02-26 with insets showing the location of several coronal emission lines. In terms of explosive transients, coronal lines have been interpreted in terms of dissipation of the energy of a shock wave in the circumstellar envelope. If collisional ionization is the dominant mechanism, then the presence of these lines implies a temperature of the emitting material of $10^5 - 10^6$ K (Bryans et al. 2009) and pre-shock ionization of the circumstellar medium by X-ray emission. For SN 2021adxl, we do not detect [Fe xiv] $\lambda 5303$ (see inset in Fig. 15), while [Fe x] $\lambda 6375$ is strong meaning the CSM temperature is likely $\lesssim 2 \times 10^6$ K (Jordan 1969; Turatto et al. 1993).

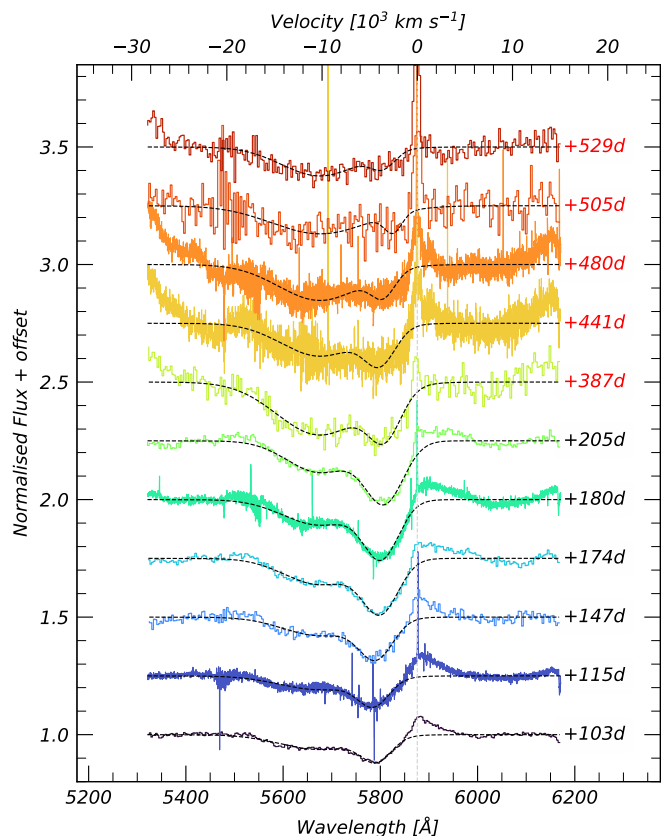


Fig. 14: Evolution of He I $\lambda 5876$ line. Each profile is continuum-subtracted. A double Gaussian absorption profile is fitted to the blue side of each spectrum, and is given by the dashed black line. We do not attempt to include the components in emission but note that the emission feature at rest wavelength narrows with time.

3. Host environment of SN 2021adxl

SN 2021adxl exploded in a blue luminous host, composed of a bright star-forming environment in the north-east, and an extended diffuse tail to the south-west (see Fig. 16). This unique morphology is coined a “tadpole” (Elmegreen et al. 2012). The blue compact northern region implies a high star-formation rate (SFR) (Botticella et al. 2012; Binder & Povich 2018), and is a likely location for massive stars and a place where CCSNe occur.

To further understand the host environment of SN 2021adxl, the software package PROSPECTOR version 1.1 (Johnson et al. 2021a) was used to analyse the spectral energy distribution from the host.

We retrieved science-ready coadded images from the *Galaxy Evolution Explorer* (GALEX) general release 6/7 (Martin et al. 2005), the Panoramic Survey Telescope and Rapid Response System (Pan-STARRS, PS1) DR1 (Chambers et al. 2016b) and images from the Wide-Field Infrared Survey Explorer (WISE; Wright et al. 2010) processed by Lang 2014. We measured the brightness of the host using LAMBDA⁹ (Lambda Adaptive Multi-Band Deblending Algorithm in R; Wright et al. 2016) and the methods described in Schulze et al. 2021. We also extract the photometry of the isolated star-forming region, in which the SN occurred. Table 3 the measurements in the different bands, and Table 4 focuses on the bright star forming knot.

⁹ <https://github.com/AngusWright/LAMBDA>

Instrument/Filter	Brightness
GALEX/FUV	17.71 ± 0.07
GALEX/NUV	17.75 ± 0.03
PS1/g	17.26 ± 0.05
PS1/r	17.21 ± 0.06
PS1/i	17.11 ± 0.04
PS1/z	17.12 ± 0.34
PS1/y	17.19 ± 0.05
WISE/W1	18.13 ± 0.10
WISE/W2	18.50 ± 0.20

Table 3: Photometric measurements of the host of SN 2021adxl. All magnitudes are in the AB system and not corrected for extinction.

Instrument/Filter	Brightness
GALEX/FUV	18.00 ± 0.08
GALEX/NUV	18.11 ± 0.05
PS1/g	17.97 ± 0.01
PS1/r	18.14 ± 0.01
PS1/i	17.93 ± 0.01
PS1/z	17.95 ± 0.03
PS1/y	18.12 ± 0.02

Table 4: Photometry of the isolated star-forming region where SN 2021adxl exploded. All magnitudes are in the AB system and not corrected for extinction.

We model the observed spectral energy distribution (black data points in Figure 18) with the software package PROSPECTOR version 1.1 (Johnson et al. 2021b).¹⁰ We assume a Chabrier IMF (Chabrier 2003) and approximate the star formation history (SFH) by a linearly increasing SFH at early times followed by an exponential decline at late times [functional form $t \times \exp(-t/\tau)$, where t is the age of the SFH episode and τ is the e -folding timescale]. The model is attenuated with the Calzetti et al. 2000 model. The priors of the model parameters are set identically to those used by Schulze et al. 2021. Figure 18 shows the observed SED (black data points) and its best fit (grey curve). The SED is adequately described by a galaxy template with a log mass of $7.80^{+0.48}_{-0.32} M_{\odot}$, a star-formation rate of $0.19^{+0.07}_{-0.07} M_{\odot} \text{ yr}^{-1}$. The mass and the star-formation rate are comparable to common star-forming galaxies of that stellar mass (grey band in Figure 17; Elbaz et al. 2007), and they are also similar to those of the host galaxy populations of SNe IIn and SLSNe-IIn from the PTF survey (Schulze et al. 2021) albeit in the lower half of the mass distribution. In the same figure, we also show the location of the star-forming knot where the SN exploded in a lighter shade. This region has a somewhat lower specific star-formation rate (i.e., star-formation rate normalised by galaxy mass) than of the entire galaxy but consistent within errors.

We focus on the narrow emission lines and the auroral emission lines associated with the underlying host (see review by Kewley et al. 2019, and references therein). The final X-shooter spectrum is utilised due to its long exposure time, and therefore higher S/N, although many of these diagnostic lines are present

¹⁰ PROSPECTOR uses the FLEXIBLE STELLAR POPULATION SYNTHESIS (FSPS) code (Conroy et al. 2009) to generate the underlying physical model and PYTHON-FSPS (Foreman-Mackey et al. 2014) to interface with FSPS in PYTHON. The FSPS code also accounts for the contribution from the diffuse gas based on the CLOUDY models from Byler et al. (2017). We use the dynamic nested sampling package DYNESTY (Speagle 2020) to sample the posterior probability.

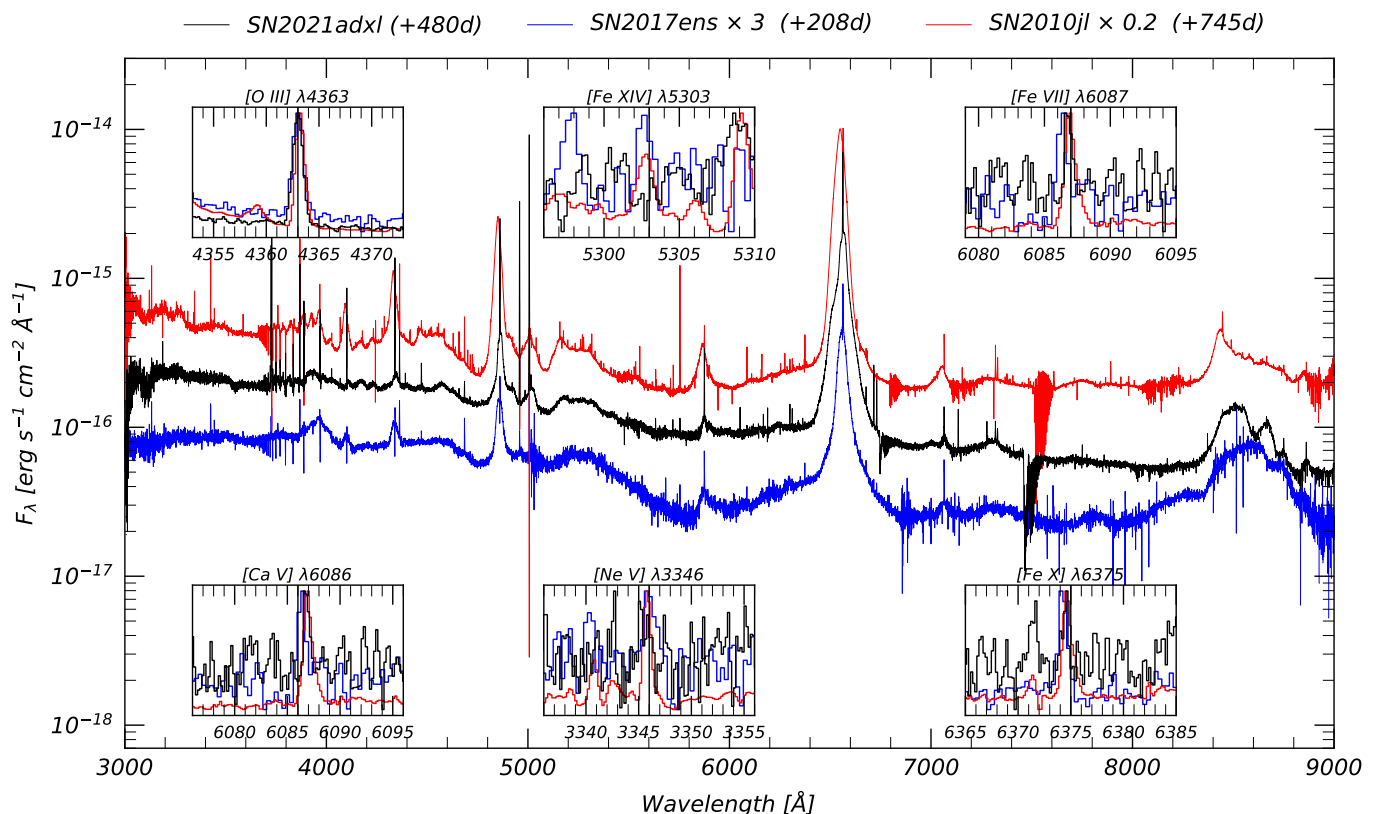


Fig. 15: Comparison of SN 2021adxl to the Type IIn SN 2010jl (Fransson et al. 2014), as well as the transitional Type Ic-BL/IIn SN 2017ens (Chen et al. 2018). The insets highlight the wavelength range around known coronal emission lines. Each inset has been normalised to the peak of each respective emission line. Interacting transients are expected to produce a significant X-ray flux, which can be manifested in coronal line emission. Although these observations are rare (due to the late time of high resolution spectra at late time), high-ionisation emission features may be common in late time spectra of interacting SNe.

in all X-shooter spectra. As seen in Fig. 26, the late time X-shooter spectra contain numerous narrow emission lines that are typically associated with H II regions. These narrow lines can provide insight into the metallicity (Z), the amount of dust, the electron temperature (T_e) and density (n_e), the age of the nebula, and the rate of star formation. However transient flux is still clearly present in our latest X-shooter spectrum. We extract a trace in the 2D spectrum from a region offset from SN 2021adxl in order to minimise the contamination from SN 2021adxl, while still detecting weak lines needed for abundance measurements, given in Fig. 19. A single narrow Gaussian emission line is fitted to each emission feature, while simultaneously fitting a pseudo-continuum. This offset spectrum still displays a weak offset broad component seen in $H\alpha$, so the following measurements (i.e. those that rely on hydrogen emission lines) may be slightly overestimated due to transient contamination. Investigating the Balmer decrement, we find $H\alpha/H\beta \approx 2.5 \pm 0.2$ and $H\gamma/H\beta \approx 0.47 \pm 0.07$, consistent with negligible interstellar reddening, as would be expected from the blue appearance of the surrounding environment, see Fig. 16.

We measure values for T_e and n_e using PyNEB¹¹ (Luridiana et al. 2014) using [O III] $\lambda 4363/\lambda 5007$ as a temperature sensitive probe, and [O II] $\lambda 3726/\lambda 3729$, and [S II] $\lambda 6731/\lambda 6716$ as density-sensitive probes, see Fig. 20. Encouragingly, we find similar results as for the abundance indicators above with $T_e \approx$

16000 K, $n_e \approx 55 \text{ cm}^{-3}$. Using [O II] and [O III], we can constrain T_e and n_e well, whereas the n_e is not well constrained by [S II], again likely due to the low density environment limit of 1.5 (Osterbrock & Ferland 2006). We search for other features to use within PyNEB, but found no other significant diagnostic lines. These may be due to the high ionising host flux, inhibiting these emission lines, or due to the low inferred densities. Using PyNEB, we find a metallicity of $12 + \log((\text{O} + \text{O}^{++})/\text{H}) = 7.61 \text{ dex}$ ($0.08 Z_\odot$), taking the solar value to be $12 + \log(\text{O}/\text{H})_\odot = 8.69 \text{ dex}$ (Asplund et al. 2021) and assuming the O II temperature dependence from Stasińska 1982.

To compare the explosion site with those of other SNe IIn, we also investigate abundance indicators using the narrow $H\alpha$ and $H\beta$ components, such as the commonly adopted N2 and O3N2 techniques (Pettini & Pagel 2004). These methods use the [N II] $\lambda 6583$ emission line which is detected in our +480d X-shooter spectrum, but has a low $S/N \lesssim 5$, and has complex underlying flux, due to the broad $H\alpha$ profile. Although there is some scatter in the derived metallicities, all methods strongly point towards a very low metallicity environment of $0.05 - 0.2 Z_\odot$.

Tables 5 and 6 give the results from the various abundance methods to determine the metallicity of the underlying environment around SN 2021adxl. Similar results (i.e. low metallicity) are found using the transient dominated spectrum from 2023-02-26 (e.g. Fig. 26), although to irrefutably confirm the metal-

¹¹ <http://research.iac.es/proyecto/PyNeb/>

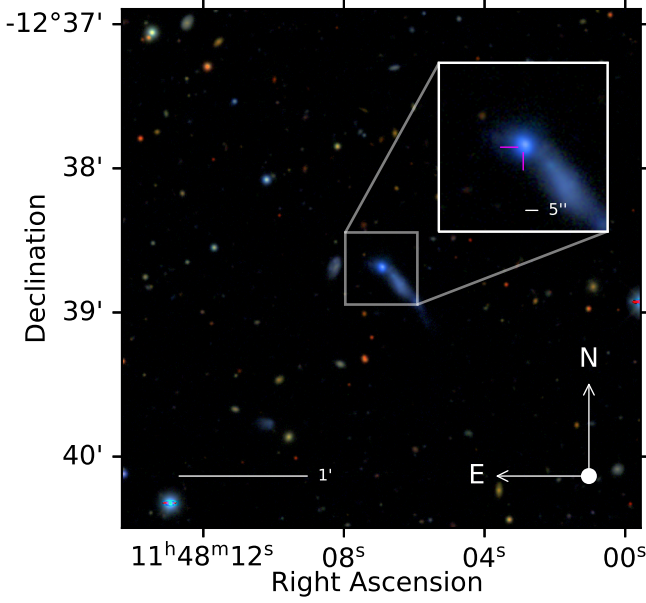


Fig. 16: Composite (*gri*) color image of the host galaxy of SN 2021adxl obtained from the DESI Legacy Surveys (Dey et al. 2019). SN 2021adxl (not visible in this image) exploded in the North-East part of its host, in a bright star-forming area. The inset provides a zoom-in of the explosion site, where the position of SN 2021adxl is marked by the crosshair.

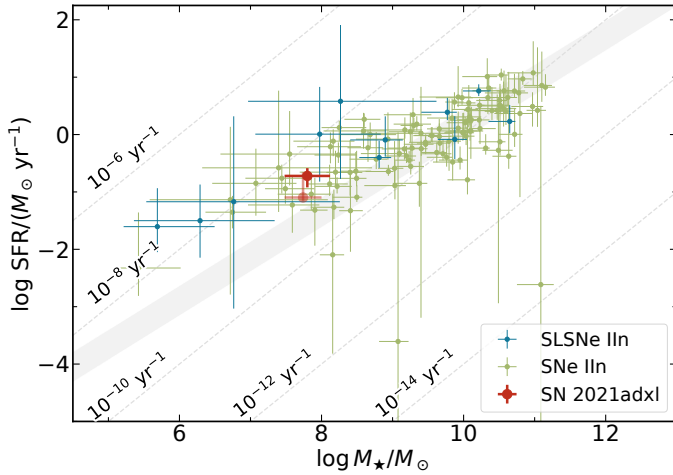
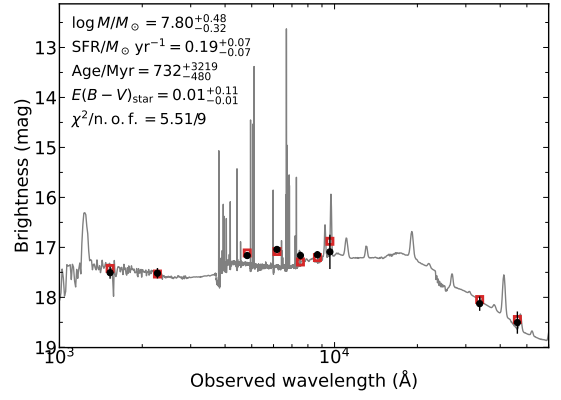
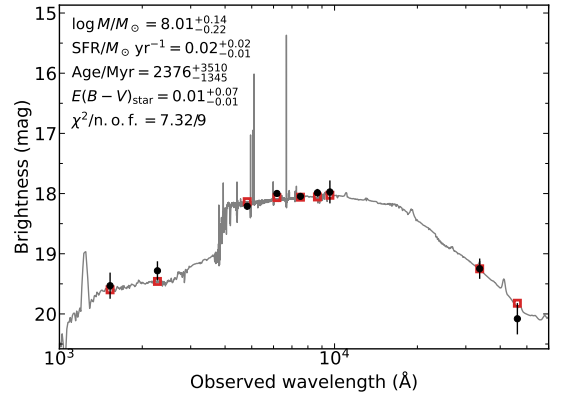


Fig. 17: The star-formation rate and stellar mass of the host galaxy of SN 2021adxl (dark red) and of the bright star-forming region where the SN exploded (light shade) in the context of SN-IIn and SLSN-IIn host galaxies from the PTF survey (Schulze et al. 2021). The host galaxy of SN 2021adxl lies in the expected parameter space of SN-IIn and SLSN-IIn host galaxies but in the lower half of the mass and SFR distributions. Its specific star-formation rate (SFR / mass) is slightly larger than the typical star-forming galaxies (grey band) but lower than for an average SLSN host galaxy.

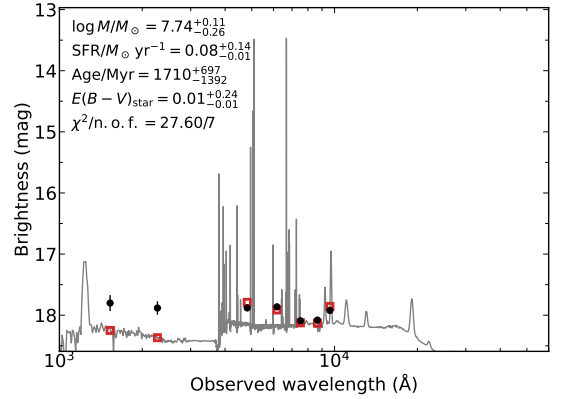
licity of the host, we require late time spectral templates once SN 2021adxl has faded.



(a) Flux from the host, including the flux from the bright head and the diffuse tail.



(b) Flux from diffuse tail to the south-west.



(c) Flux from bright star forming head to the north-west.

Fig. 18: Spectral energy distribution of the host galaxy from 1000 to 60,000 Å (black dots). The solid line displays the best-fitting model of the SED. The red squares represent the model-predicted magnitudes. The fitting parameters are shown in the upper-left corner. The abbreviation ‘n.o.f.’ stands for the number of filters. We perform measurements on the entire host flux (upper panel), the faint tail (middle panel) and the star forming blob (lower panel) where SN 2021adxl exploded.

4. Modelling the H α profile

In order to understand the formation of the hydrogen emission lines, we note two distinct features, one is the offset flat topped emission profile, which suggests of a thin emitting shell (Jerkstrand 2017) and the second is the red-ward, extended wings,

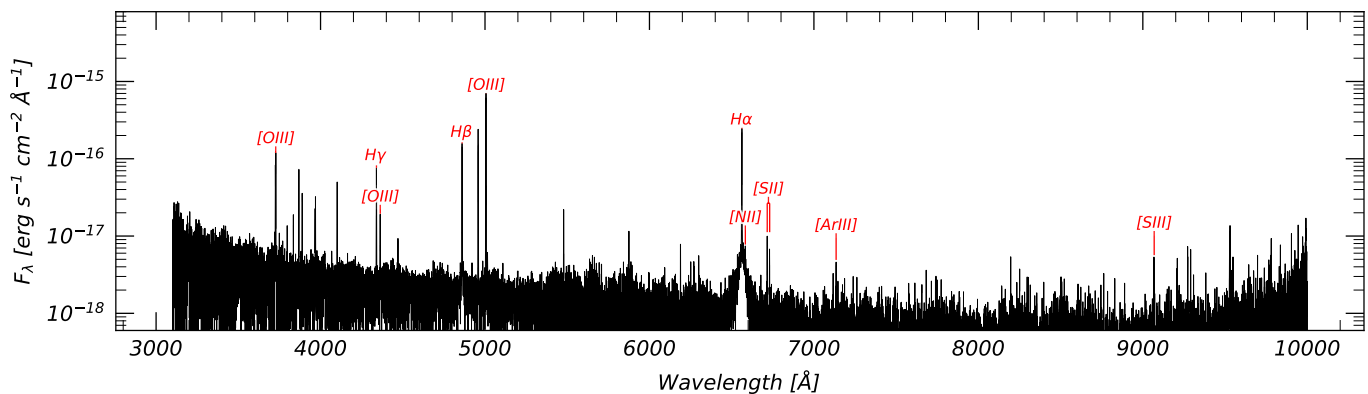


Fig. 19: Spectrum extracted from a region offset from the X-shooter spectrum taken on 2023-02-26. Emission lines used in metallicity, T_e and n_e measurements are marked in red. We note transient flux is still present in the spectrum, as is seen by the broad appearance of $H\alpha$ and $H\beta$.

Table 5: Measured parameters for several emission lines in the VLT/XShooter spectrum taken on 2023-02-26 (+480d). Flux has been corrected for MW extinction. Errors for each measurement are given in parentheses. Errors on the Equivalent Width (EW) are from Cayrel (1988, their Eq. 6). Note for the Hydrogen emission lines, we measure the flux from the narrow component only.

	Flux [$\text{erg s}^{-1} \text{cm}^{-2}$]	FWHM [km s^{-1}]	EW [\AA]
H λ 4340	$3.834 (0.020) \times 10^{-16}$	36.408 (0.164)	-12.790 (0.003)
H λ 4861	$8.351 (0.019) \times 10^{-16}$	37.061 (0.156)	-19.417 (0.002)
H λ 6563	$2.047 (0.005) \times 10^{-15}$	27.633 (0.182)	-14.439 (0.001)
[Ar III] λ 7135	$2.246 (0.093) \times 10^{-17}$	20.292 (0.332)	-2.494 (0.028)
[N II] λ 6583	$1.495 (0.245) \times 10^{-17}$	19.677 (0.626)	-0.159 (0.109)
[O III] λ 4363	$6.503 (0.199) \times 10^{-17}$	34.855 (0.327)	-2.242 (0.020)
[O III] λ 5007	$3.079 (0.005) \times 10^{-15}$	34.975 (0.202)	-139.444 (0.001)
[O II] λ 3726	$4.396 (0.043) \times 10^{-16}$	37.360 (0.158)	-13.415 (0.006)
[O II] λ 3729	$6.253 (0.087) \times 10^{-16}$	35.613 (0.209)	-19.163 (0.009)
[S III] λ 9069	$5.686 (0.095) \times 10^{-17}$	22.275 (0.157)	-8.518 (0.011)
[S II] λ 6716	$7.301 (0.119) \times 10^{-17}$	24.933 (0.558)	-6.277 (0.011)
[S II] λ 6731	$5.263 (0.102) \times 10^{-17}$	24.194 (0.472)	-4.766 (0.013)

Table 6: Metallicity measurements for SN 2021adxl using various abundance indicators found in literature.

	$12 + \log(\text{O}/\text{H})$	Z/Z_\odot
PyNeb	7.61	0.08
N2	7.76	0.12
O3N2	7.95	0.18

which are characteristic of electron scattering (Huang & Chevalier 2018).

The collision of the fast moving ejecta with the slower moving CSM results in the formation of a dense shell of material. This shell is made up of swept-up, shock-heated gas from the circumstellar medium and can efficiently cool to relatively low temperatures compared to the high-energy, shock-heated gas found in other parts of the supernova ejecta. This cool dense shell (CDS) of material is bound between the outward moving forward shock and receding reverse shock (Chugai et al. 2004; Smith 2017a). Diffusion of radiation from this shocked shell produces the main continuum (e.g. red line of Fig. 6) as well as the intermediate ($\sim 10^3 \text{ km s}^{-1}$) components of $H\alpha$.

Under the assumption that the $H\alpha$ profile arises from photons emitted from the CDS that undergo multiple scattering events as they travel outwards through the surrounding media, a model of electron scattering is explored. A Monte Carlo code was developed¹² in order to follow photons emitted from a thin shell as they travel through a diffuse medium. The code is based on the work by Pozdnyakov et al. 1983 and similar codes have been employed in previous works on interacting SNe (e.g., Fransson et al. 2014; Taddia et al. 2020). In this model, photons are emitted with an emissivity η , which varies with the electron density as $\propto n_e^2$ and $n_e \propto r^{-2}$. Photons are followed until they escape the scattering medium, with a probability $\propto e^{-\tau_e}$. We include an occulting photosphere, meaning that any escaping photons moving away from the observer are excluded. The optical depth, electron temperature, and radius are degenerate in these electron scattering models (see Huang & Chevalier 2018, for details), and are left as restricted parameters. While this is nonphysical for a SN explosion as these parameters evolve with time, the models can be used to understand the formation of the $H\alpha$ profile, as well as to further understand the main properties of the SN and, in particular, the shock velocity (V_{shock}) and mass-loss rate (\dot{M}).

¹² <https://github.com/Astro-Sean/escatter>

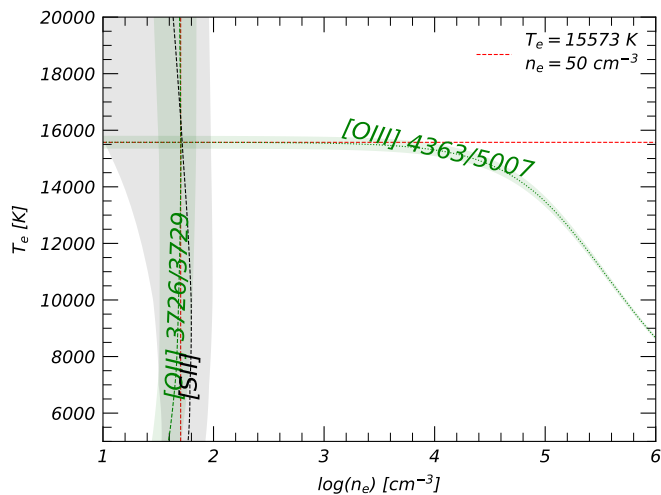


Fig. 20: Emission-line temperature and density diagnostic plot from PYNEB using [O III] $\lambda 4363/\lambda 5007$ as a temperature sensitive probe, and [O II] $\lambda 3726/\lambda 3729$, and [S II] $\lambda 6731/\lambda 6716$ as density-sensitive probes.

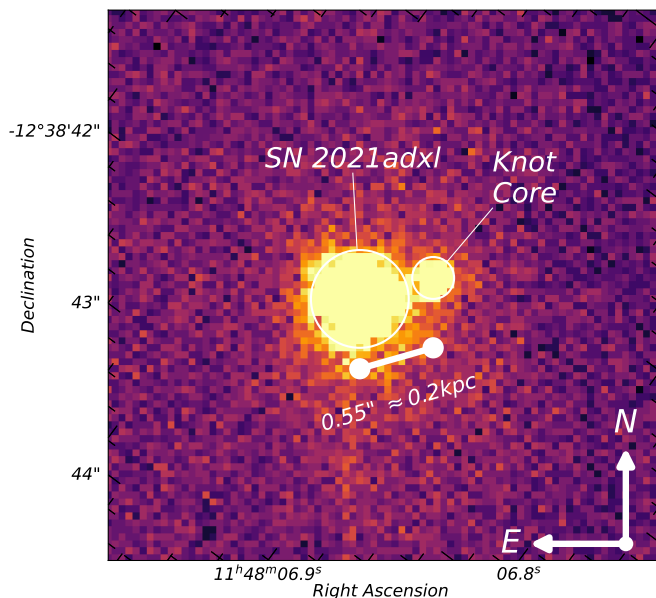


Fig. 21: A $4'' \times 4''$ cutout from the HST/STIS acquisition images from 2022-04-11 (+159 d) including SN 2021adxl as well as the compact bright star forming knot. SN 2021adxl is separated from this compact knot by roughly half an arcsecond, or a projected distance of ~ 0.2 kpc.

Figure 22 shows the first epoch X-shooter spectrum with the best fitting electron scattering model. The model matches the spectrum well, capturing the blue shoulder as well as the extended red wing. However, the model fails to capture the features around rest wavelength. This likely represents emission from slowly moving material surrounding the SN ejecta, as well as emission from the host.

Similar to Fig. 22, Fig. 23 shows the best fitting model for the earliest X-shooter spectrum, but with additional two Gaussian components, which likely reflect emission from the host and from CSM material far away from the shock (which we do

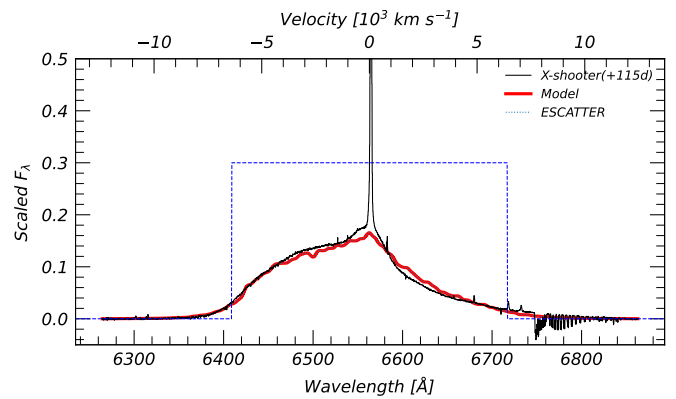


Fig. 22: $H\alpha$ profile from the VLT/X-shooter spectrum (black) with the best fitting electron scattering model (red) for a given input spectrum (blue). The model matches the blue and red sides of the emission line well, but leaves an intermediate and narrow emission component at the central wavelength.

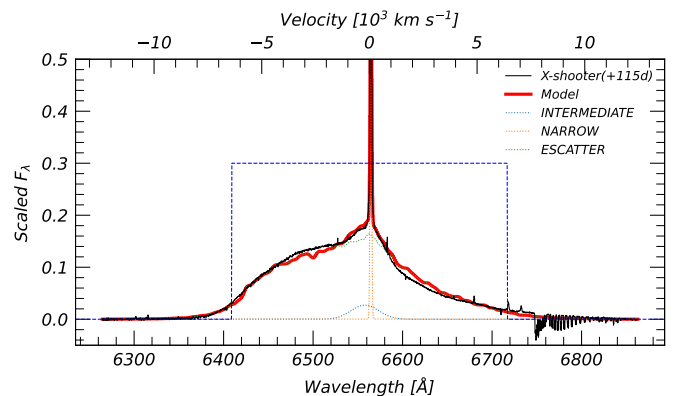


Fig. 23: Same as Fig. 22, but now including an additional intermediate and narrow Gaussian emission component. These three components can reproduce the entire $H\alpha$ profile well.

not include in our models). As demonstrated in Fig. 12, the $H\alpha$ profile evolves with time, and most notably, its blueward component moves toward the central wavelength. Using a grid of electron scattering models with an input spectrum representing a thin emitting shell, we are able to match the best fit model to the $H\alpha$ profile for each spectrum (excluding the SEDM spectra due to their low resolution) to better understand how this blueward feature evolves. Figure 24 gives the results of the evolution of the velocity needed to produce the $H\alpha$ profile at each epoch. During Phase 1, the velocity evolution is well fitted by:

$$V_{\text{shock}} = 6625 \times \left[\frac{t}{100 \text{ days}} \right]^{-0.37} \text{ km s}^{-1}. \quad (1)$$

At the beginning of Phase 2, the model velocities are much lower and no longer follow Eq. 1. Models fitted in Phase 2 show more scatter in their inferred velocity, and one should note the additional complexity of the $H\alpha$ profile at this time as shown in Fig. 12.

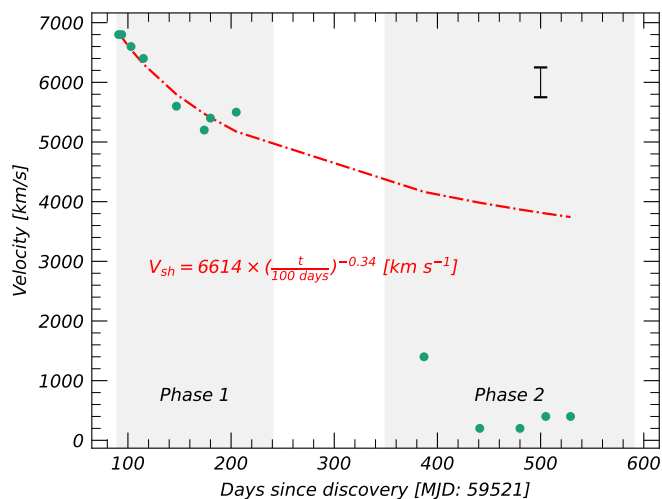


Fig. 24: Input velocities of the best-fitting models needed to fit the $H\alpha$ profile evolution. Velocities during Phase 1 are fitted with an exponential decline, given in red. During Phase 2, the velocities are lower and no longer follow the trend seen in Phase 1. This is likely due to the forward shock becoming optically thin, which is also seen in the faster decay rate in the bolometric lightcurve seen in Fig. 3. The errorbar in the upper right denotes the velocity grid-resolution of the input spectra.

4.1. Modelling the ejecta-CSM interaction

The dominating energy input during the evolution of Type II n SNe is due to the interaction between the SN ejecta and the surrounding CSM (Dessart et al. 2015). The diversity of the mass, velocities, and geometry of this interacting material are likely responsible for the heterogeneous appearance of this subclass (Chatzopoulos et al. 2012; Nyholm et al. 2020; Khatami & Kasen 2023). The total luminosity generated by ejecta-CSM interaction can be high because a radiative shock is a very efficient engine to convert kinetic energy into radiation at optical wavelengths. The luminosity of the CSM interaction is dependent on the velocity at which CSM enters the forward shock and on the progenitor’s mass-loss rate (\dot{M}), and is typically given by:

$$L_{\text{shock}} = 2\pi\rho_{\text{CSM}}r_{\text{shock}}^2 V_{\text{shock}}^3 = \epsilon \frac{\dot{M}}{2 v_{\text{wind}}} V_{\text{shock}}^3 \text{ erg s}^{-1} \quad (2)$$

assuming a steady mass-loss rate for the CSM (Wood-Vasey et al. 2004) and a 50% conversion efficiency ($\epsilon = 0.5$). It is often difficult to determine the shock velocity from the line profiles given the uncertainty to which extent electron scattering plays a role in determining the widths of the intermediate lines (see discussion by Smith 2017a). SN 2021adxl offers a unique test to measure the degree to which electron scattering plays a role, as discussed in Sect. 4, and therefore to gain insight into the ejecta-CSM interaction.

Using Eqs. 1 and 2, we fit the Phase 1 portion of the lightcurve with the mass-loss rate \dot{M} as a free parameter. The CSM velocity is taken to be $\sim 250 \text{ km s}^{-1}$, as seen in the earliest spectrum, see Fig. 7, as well as the HST/COS spectrum given, see Fig. 8. As discussed in Sect. 4, the blue component of the $H\alpha$ profile is likely caused by line scattering from a somewhat optically thin CDS. One interpretation of this is that photons are emitted from the outer regions of the CDS, and while travelling

radially outwards, scatter off material swept up by the forward shock.

It is important to note that the measurements of the shock velocity as provided in Eq. 1 are not based on the photometric evolution, but rather model fitting of the $H\alpha$ profile. The exponent for the shock velocity evolution in Eq. 2 is responsible for the slope, and it is encouraging that the resulting fit in Fig. 25 matches the bolometric evolution so well. Equations 1 and 2 fits the luminosity of Phase 1 but this does not extend to Phase 2, where a faster, apparently linear, decline is seen. Extrapolating both trends, we expect a break around +300 d. Following Eq. 2, a steady state mass-loss rate of $4 - 6 \times 10^{-3} M_{\odot} \text{ yr}^{-1}$ is required to provide the necessary luminosity if powered solely by shock interaction. Additionally, it is possible to fit a second decline similar to Eq. 2 to Phase 2 with a quicker velocity decline with an exponent of ≈ -1.3 , however it is difficult to constrain this.

The use of Eq. 2 is likely an oversimplification but provides an estimate to the the mass-loss rate from the progenitor shortly before the SN explosion. A mass-loss rate of $10^{-3} M_{\odot} \text{ yr}^{-1}$ is consistent with reported values for other interacting SNe (Taddia et al. 2013; Ofek et al. 2014; Fransson et al. 2014; Moriya et al. 2014, 2023) as well as the values often assumed for Luminous Blue Variable (LBV) progenitors (Trundle et al. 2008; Dwarkadas 2011; Groh et al. 2013; Smith 2017b; Weis & Bommans 2020) as discussed further in Sect. 5.3.

As shown in Fig. 2, SN 2021adxl undergoes a steeper decline after Phase 1 and the trend seen in Fig. 24 may be related, perhaps reflecting a change in CSM density, distribution, or opacities, e.g. see discussion by for SN 2010jl (Ofek et al. 2014; Moriya 2014). This is also observed in the evolution of the $H\alpha$ profile in Fig. 12, when the overall profile narrows during Phase 2, likely reflecting a lower optical depth for material ahead of the shock from, meaning less scattering events (Huang & Chevalier 2018) and less broadening of the emission profile.

If we assume the ejecta-CSM interaction ceases when the shock reaches the edge of the dense CSM at a time t_{end} , we can estimate the radial extent of this material (d_{CSM}) using:

$$d_{\text{CSM}} = \int_{t_{\text{start}}}^{t_{\text{end}}} (t - t_{\text{start}}) \times V_{\text{shock}}(t) dt, \quad (3)$$

where t_{start} is the time at which the SN ejecta collides with the CSM, launching the forward shock into the dense CSM, and we use $V_{\text{shock}}(t)$ from Eq. 1. We do not have a constraint on the explosion date so we can not be certain on the duration of CSM interaction.

We make an conservative estimation of d_{CSM} by assuming that $t_{\text{start}} = 100$ days, $t_{\text{end}} = 300$ days and $t_{\text{duration}} \approx 200$ days (although this value may be a factor of 2 or more greater), the time-frame for which Eq. 1 is likely to be valid i.e the duration of Phase 1. This gives an approximate size of d_{CSM} of $8 \times 10^{17} \text{ cm}$ (this is more than an order of magnitude larger than that reported for SN 2010jl for example Dwek et al. 2021) meaning that the CSM travelling at $\sim 250 \text{ km s}^{-1}$ would have been ejected in the last ~ 1000 years. We can set a lower limit on the CSM mass in Phase 1, assuming a constant $\dot{M} = 4 \times 10^{-3} M_{\odot} \text{ yr}^{-1}$, homologous distribution, and spherical symmetry, as $M_{\text{CSM}} \gtrsim 4.3 M_{\odot}$. Additionally this mass will be substantially higher if we have overestimated V_{wind} or underestimated t_{start} and t_{end} , although this is hard to quantify as we are uncertain how V_{shock} evolves for $t \lesssim 100$ days. This high CSM mass is similar to that measured for SN 2010jl ($\sim 1 - 10 M_{\odot}$; Zhang et al. 2012; Fransson

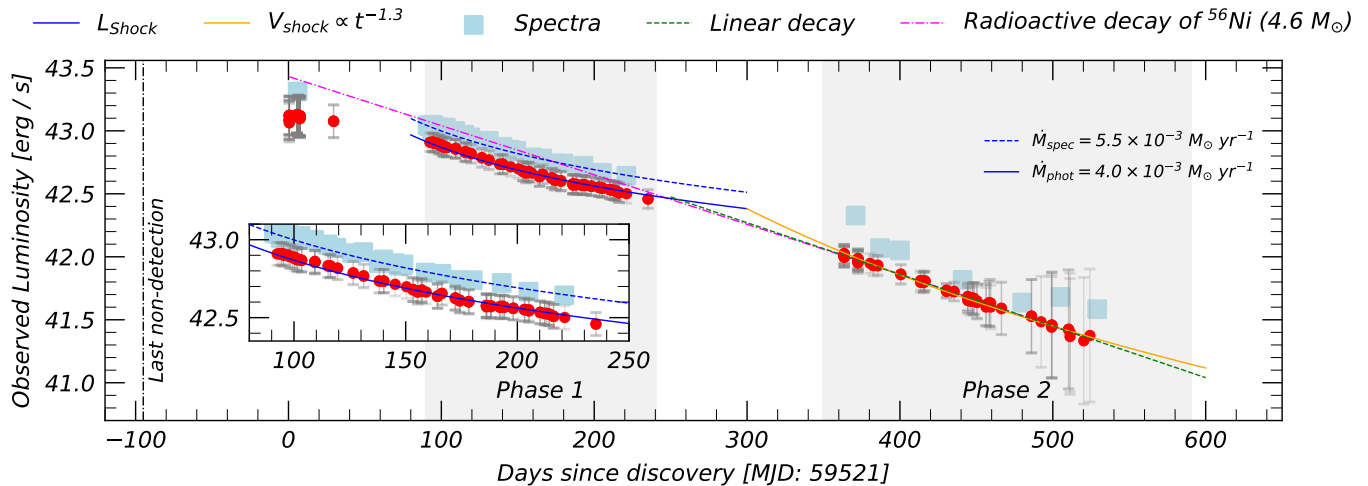


Fig. 25: Pseudo-bolometric lightcurve of SN 2021adxl. Best fitting model from Eq. 2 fitting to Phase 1 photometry (spectra) is given as the blue solid (dashed) blue line. Included in the inset is a zoom in of this phase. Both a linear decline (dashed green) and possible shock luminosity curve (solid orange) is fitted to Phase 2. The magenta line is the decay expected for radioactive nickel, fitted to Phase 2, as discussed in Sect. 4.1.

et al. 2014; Ofek et al. 2014) and is likely a contributing reason for the slow evolution seen in both transients.

Assuming SN 2021adxl to be entirely powered by radioactive decay, Fig. 25 includes the energy deposited by a mass of explosively synthesised radioactive material given by Jeffery 1999, and the mass of radioactive nickel needed would be on the order of 3-10 M_{\odot} of material. However such a mass of nickel would produce a much brighter transient, and would over-predict the luminosity evolution during Phase 1. This is obviously an over-estimate, and not expected for SN 2021adxl, as the transient is likely dominated by CSM interaction even in Phase 2. We conclude that CSM interaction likely dominates Phase 2, although there is a different CSM mass / distribution when compared to Phase 1 meaning the progenitor has undergone several mass loss episodes in the final moments before core-collapse.

5. Discussion

SN 2021adxl is an example of a nearby, bright, long-lasting interacting supernova. This allows for a rare glimpse to the late-time evolution of the transient and for this purpose we have obtained high-resolution spectra. Figure 26 provides a detailed picture of the final VLT/X-shooter spectrum taken at +480d. This highlights the weaker, narrow emission features that are typically missed when lower-resolution spectrographs are employed. For context, many narrow features discussed in this section are not detected in the NOT+ALFOSC spectra. This suggest an inefficient observing strategy for late time transient followup when only low-medium spectrum are obtained.

5.1. The nature of the SN 2021adxl's host

The $\text{Ly}\alpha$ profile seen in Fig. 8 is in contrast to the appearance of $\text{H}\alpha$ as shown in Fig. 11. While this may be an opacity effect, or possibly due to emission from material far away from the ejecta-CSM interface as mentioned above, similar profiles for $\text{Ly}\alpha$ have been seen for population of compact, star-forming galaxies at $z \sim 0.2 - 0.3$, also known as “green peas” (GP) galaxies (Cardamone et al. 2009). These GP galaxies have a high

[O III] λ 5007 / [O II] λ 3726 ratio, high equivalent width in O III emission lines (See Table. 5 Cardamone et al. 2009), and are typically sub- solar metallicity (Orlítóva et al. 2018; Liu et al. 2022). Our PROSPECTOR measurements also find a mass consistent with GP ($\sim 10^8 M_{\odot}$; Cardamone et al. 2009). Although due to its proximity, the host of SN 2021adxl would be classified as a Blueberry galaxy rather than a Green Pea (Liu et al. 2022).

As shown in Fig. 8, the $\text{Ly}\alpha$ shows a unique profile that is not clearly seen in any other emission profile. The profile may resemble a P-Cygni emission profile, typically observed in stellar winds and SNe, or a doubled peaked emission profile with an absorption trough at center wavelength. We note the similarities of the HST/STIS $\text{Ly}\alpha$ profile to that observed in GP galaxies (e.g. Yang et al. 2016; Orlítóva et al. 2018; Henry et al. 2018). In this case, the asymmetric profile is thought to be due to resonant scattering of $\text{Ly}\alpha$ photons off neutral hydrogen atoms, which is dependant on the intervening material and fraction of escaping ionizing radiation. This would also point that the broad feature in Fig. 9 would be Mg II $\lambda\lambda$ 2796, 2803 (Henry et al. 2018), originating from the host and not SN 2021adxl, although does not explain the observed wavelength offset.

5.2. Type IIIn SNe exploding in metal poor environments

Perhaps greater insight may be gained from the local environment around SN 2021adxl. As mentioned in Sect. 3, SN 2021adxl occurred in a bright star-forming region at the end of an elongated intensity distribution. We find that the local environment has a very low metallicity of $0.06 Z_{\odot}$. This is similar to the environments for SN 2010jl (Stoll et al. 2011) and SN 2013L (Taddia et al. 2020), as well as for other Type IIIn SNe (Habergham et al. 2014; Moriya et al. 2023).

Figure 27 compares the measured metallicities for the host of SN 2021adxl to a sample of values for hosts of Type IIIn SNe (Habergham et al. 2014; Moriya et al. 2023), Type II SLSN (Leloudas et al. 2015), as well as both Type I and II SLSNe (Perley et al. 2016). SN 2021adxl is at drastically lower metallicity than the sample of Type IIIn SNe (e.g. samples from Habergham et al. 2014; Moriya et al. 2023), and also lower than for Type

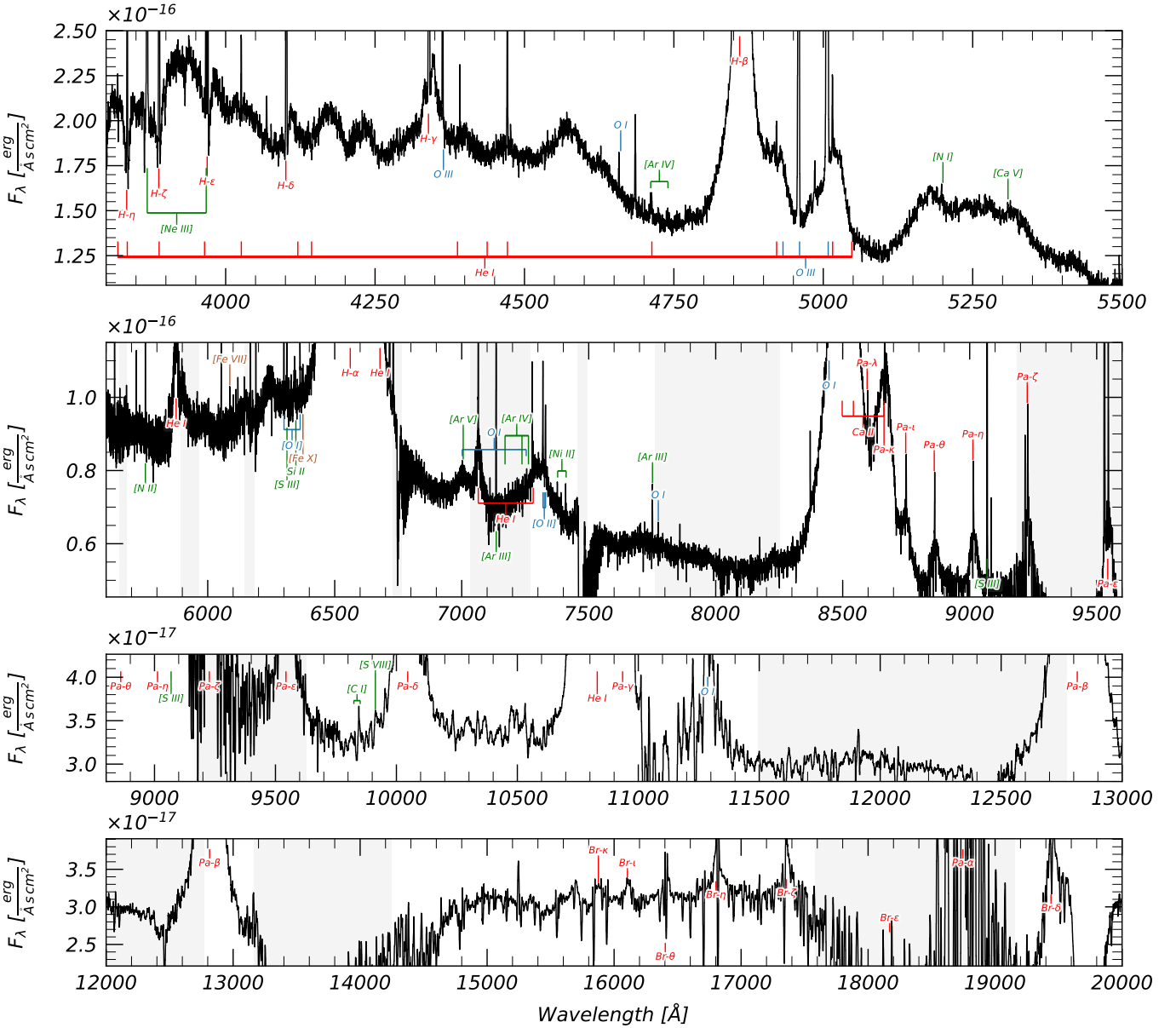


Fig. 26: VLT/X-shooter for SN 2021adxl taken on 2023-02-26 (+480d). The spectrum has been fluxed calibrated to the r -band and each panel highlights a wavelength range which (roughly) covers the near UV, optical, and near-IR. Telluric bands are marked by the grey area. The bottom two panels have been smoothed using a Savgol filter for clarity.

II SN hosts (except perhaps for SN 2015bs; Anderson et al. 2016, 2018). The sample of Moriya et al. 2023 does include SN 2016iaf having $12 + \log(\text{O}/\text{H}) = 7.48 \pm 0.81$ using the D16 method (Dopita et al. 2016), although this metallicity is outside the reported validity range for D16.

Moriya et al. 2023 find that Type IIn SNe with a higher peak luminosity occur in environments with lower metallicity and young stellar environment. Although SN 2021adxl is beyond the range explored by Moriya et al. 2023, the location and metallicity of the environment SN 2021adxl occurred in may explain its brightness. The conjecture that more luminous IIn's are found in less metal-enrichment environments is in conflict with results from Leloudas et al. 2015, Perley et al. 2016 and Schulze et al. 2018, 2021. Figure 27 is contradicting this scenario, too. The SLSN-II sample spans the full range of metallicities (e.g. sample from Leloudas et al. 2015, in Fig. 27). The fact that they are

super-luminous, and therefore more luminous than SN 2021adxl implies that their environments should on average be less metal enriched than of SN 2021adxl, in contradiction with the result of Moriya et al. 2023. Additionally, Moriya et al. 2023 find a strong inverse correlation between peak luminosity and metallicity, which may possibly explain the brightness of SN 2021adxl although the peak magnitude would be overestimated by almost 2 magnitudes (see Fig. 1 of Moriya et al. 2023).

5.3. Progenitor of SN 2021adxl

A major problem in supernova science concerns identifying the progenitors of Type IIn SNe. Progress is further hindered by the lack of clear nebular emission line signatures (which may reveal clues to the progenitor e.g. Fraser et al. 2013; Jerkstrand et al. 2020). We are therefore often left with modelling the lightcurve

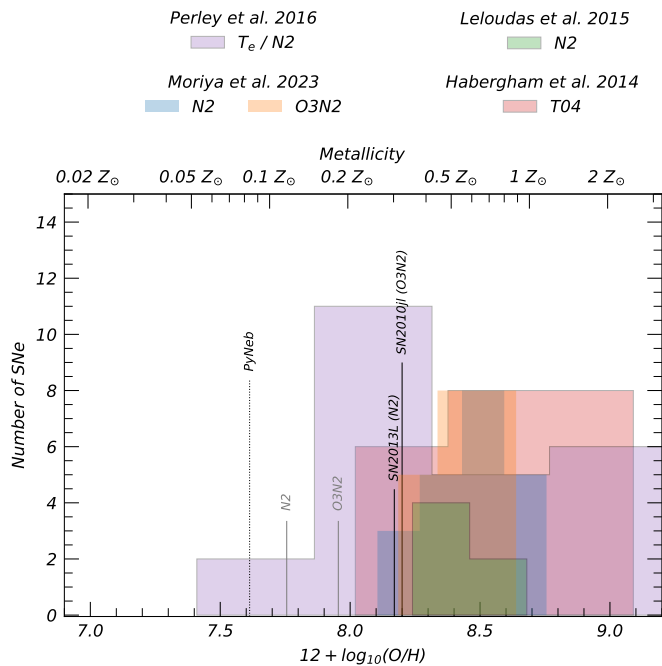


Fig. 27: Metallicity measurements for the environment around SN 2021adxl using the VLT/X-shooter spectrum on 2023-02-26 (+480d). Histograms are measured metallicities for hosts of Type II In SNe (Habbergham et al. 2014; Moriya et al. 2023), Type II SLSNe (Leloudas et al. 2015), as well as both Type I and II SLSNe (Perley et al. 2016) using various methods, denoted in the legend, and detailed in Sect. 3. Vertical lines mark measured values for SN 2021adxl using different methods (see text). We also mark the reported metallicity for SN 2010jl at $Z \approx 0.32 Z_{\odot}$ (Stoll et al. 2011) and for SN 2013L at $Z \approx 0.30 Z_{\odot}$ (Taddia et al. 2020).

and spectra, which in the case of interacting transients, are dominated by the effects of interaction, obscuring the signatures of any explosion mechanism (Arcavi et al. 2017; Woosley 2018).

There are no progenitor detections of SN 2021adxl, so we must rely on indirect methods. In Sect. 4.1, we concluded that SN 2021adxl can be powered by the ejecta colliding with a previous wind with $\dot{M} \approx 10^{-3} M_{\odot} \text{ yr}^{-1}$. This mass-loss rate regime is often reserved for LBVs during their outburst stages (Lamers 1989; Weis 2001; Vink 2008; Smith 2013), and additionally the inferred wind velocity is also similar to that observed among Galactic LBVs (Weis 2001).

Such high mass-loss rates are commonly inferred for Type II In SNe (Moriya et al. 2014), although it is difficult to have a physical mechanism that can lead to this amount of mass ejected (Fuller 2017; Tsang et al. 2022). Such a high steady state mass-loss rate is unlikely to be obtained from a single star. Using Eq. 20 from Björklund et al. 2021, a massive hot star would require a luminosity of $L \approx 10^{7.2} L_{\odot}$ to achieve a steady state mass-loss rate of $10^{-3} M_{\odot} \text{ yr}^{-1}$ at a metallicity of $0.2 Z_{\odot}$ (this is the lower validity range from Björklund et al. 2021), which would likely exceed the Eddington luminosity of a single star. This is similar to the luminosity expected from the 1840 Giant Eruption of Eta Carinae (Davidson & Humphreys 2012), where it is thought that binary interaction was the cause of the eruption (see Smith 2011, for a possible scenario).

The involvement of a companion in the progenitor history is an often explored formation channel for Type II In SNe (Chatzopoulos et al. 2012; Justham et al. 2014; Zapartas et al. 2019), as most massive stars are expected to be born and interact with a binary companion (Sana et al. 2012; Zapartas et al. 2019). The environments of Type II In do not show dramatic differences when compared to normal Type II (Kelly & Kirshner 2012), suggesting there is no significant environment dependence for these two sub types, and (possibly) they are influenced by the present (or absence) of a companion. At the time of writing SN 2021adxl no obvious signatures of binarity (e.g. pre-explosion variability, multi-peaked emission lines) are detected. While SN 2021adxl is a luminous Type II In supernova, it does not reach the often assumed -21 mag criteria of SLSNe (Gal-Yam 2012). However in the context of interacting SNe, it is not clear whether SNe II In fulfilling this criterion constitute a separate population of events (Moriya et al. 2018; Gal-Yam 2019; Nyholm et al. 2020) or whether there is a continuum of possible energetics (see Fig. 1 of Moriya et al. 2023).

6. Conclusions

We present 1.5 years of the evolution of the luminous Type II In SN 2021adxl, including four epochs of spectrum from the VLT/X-shooter. SN 2021adxl, similar to SN 2010jl, does not evolve quickly, and since discovery has only faded by ~ 4 magnitudes. This likely reflects that the forward shock, created from the ejecta-CSM interaction, is moving outwards through a dense, extended CSM environment. The effects of this environment are seen in the appearance of the $H\alpha$ emission line, which displays a persistent blue shoulder emission component. We find that this feature is due to electron scattering through an increasingly diffuse medium ahead of the forward shock. Using the evolution of this feature, we find that the post-peak evolution is dominated by the ejecta-CSM interaction. Assuming spherical symmetry and homologous density distribution, this translates to a shock wave moving through dense medium of $\geq 3 M_{\odot}$ extended out to at least $\sim 10^{17}$ cm. Between 250 and 350d, the properties of the CSM interaction changes. The light curve decay increased and the broad $H\alpha$ profile narrows, likely due to a decrease in the CSM density. This may signify a change in the evolution of the progenitor within the last $\sim 10^3$ years.

Perhaps one of the most striking features of SN 2021adxl is where it occurred. The vicinity around SN 2021adxl displayed a prominent blue appearance, and we show that this is a low density, low metallicity environment. The peak brightness of SN 2021adxl may be related to its metallicity, as more metal poor progenitors may produce bright Type II In SNe (e.g. Moriya et al. 2014). Although this is likely not the (direct) cause of the high mass loss rates, as Type II In SNe occur in heterogeneous environments, with multiple formation pathways (Ransome et al. 2022). Thanks to its proximity and (expected) slow evolution, SN 2021adxl will be observable again in early-2024, allowing for continued observations at +800 days.

Acknowledgements

S. J. Brennan and R. Lunnan acknowledge support by the European Research Council (ERC) under the European Union’s Horizon Europe research and innovation programme (grant agreement No. 10104229 - TransPIre). S. Schulze is partially supported by LBNL Subcontract NO. 7707915 and by the G.R.E.A.T. research environment, funded by Vetenskapsrådet,

the Swedish Research Council, project number 2016-06012. T. W. Chen acknowledges the Yushan Young Fellow Program by the Ministry of Education, Taiwan for the financial support. Y.-L. Kim has received funding from the Science and Technology Facilities Council [grant number ST/V000713/1].

Based on observations obtained with the Samuel Oschin Telescope 48-inch and the 60-inch Telescope at the Palomar Observatory as part of the Zwicky Transient Facility project. ZTF is supported by the National Science Foundation under Grant No. AST-2034437 and a collaboration including Caltech, IPAC, the Weizmann Institute of Science, the Oskar Klein Center at Stockholm University, the University of Maryland, Deutsches Elektronen-Synchrotron and Humboldt University, the TANGO Consortium of Taiwan, the University of Wisconsin at Milwaukee, Trinity College Dublin, Lawrence Livermore National Laboratories, IN2P3, University of Warwick, Ruhr University Bochum and Northwestern University. Operations are conducted by COO, IPAC, and UW. SED Machine is based upon work supported by the National Science Foundation under Grant No. 1106171. This work was supported by the GROWTH project funded by the National Science Foundation under Grant No 1545949. The Oskar Klein Centre is funded by the Swedish Research Council. The data presented here were obtained [in part] with ALFOSC, which is provided by the instituto de Astrofísica de Andalucia (IAA) under a joint agreement with the University of Copenhagen and NOT. The ZTF forced-photometry service was funded under the Heising-Simons Foundation grant #12540303 (PI: Graham). The Gordon and Betty Moore Foundation, through both the Data-Driven Investigator Program and a dedicated grant, provided critical funding for SkyPortal.

Data availability

The spectroscopic data underlying this article are available in the Weizmann Interactive Supernova Data Repository (WiSeREP¹³ Yaron & Gal-Yam 2012). The photometric data underlying this article are available in the online supplementary material.

References

- Anderson, J. P., Dessart, L., Gutiérrez, C. P., et al. 2018, *Nature Astronomy*, 2, 574
- Anderson, J. P., Gutiérrez, C. P., Dessart, L., et al. 2016, *A&A*, 589, A110
- Andrews, J. E., Sand, D. J., Valenti, S., et al. 2019, *ApJ*, 885, 43
- Andrews, J. E. & Smith, N. 2018, *MNRAS*, 477, 74
- Andrews, J. E., Smith, N., McCully, C., et al. 2017, *MNRAS*, 471, 4047
- Appenzeller, I. & Oestreicher, R. 1988, *AJ*, 95, 45
- Arcavi, I., Howell, D. A., Kasen, D., et al. 2017, *Nature*, 551, 210
- Asplund, M., Amarsi, A. M., & Grevesse, N. 2021, *A&A*, 653, A141
- Bellm, E. 2014, in *The Third Hot-wiring the Transient Universe Workshop*, ed. P. R. Wozniak, M. J. Graham, A. A. Mahabal, & R. Seaman, 27–33
- Bellm, E. C., Kulkarni, S. R., Graham, M. J., et al. 2019, *PASP*, 131, 018002
- Bethe, H. A. 1990, *Reviews of Modern Physics*, 62, 801
- Binder, B. A. & Povich, M. S. 2018, *ApJ*, 864, 136
- Björklund, R., Sundqvist, J. O., Puls, J., & Najarro, F. 2021, *A&A*, 648, A36
- Blagorodnova, N., Neill, J. D., Walters, R., et al. 2018, *PASP*, 130, 035003
- Botticella, M. T., Smartt, S. J., Kennicutt, R. C., et al. 2012, *A&A*, 537, A132
- Brennan, S. J., Fraser, M., Johansson, J., et al. 2022, *MNRAS*, 513, 5642
- Bryans, P., Landi, E., & Savin, D. W. 2009, *ApJ*, 691, 1540
- Burrows, A. & Vartanyan, D. 2021, *Nature*, 589, 29
- Burrows, D. N., Hill, J. E., Nousek, J. A., et al. 2005, *Space Sci. Rev.*, 120, 165
- Byler, N., Dalcanton, J. J., Conroy, C., & Johnson, B. D. 2017, *ApJ*, 840, 44
- Calzetti, D., Armus, L., Bohlin, R. C., et al. 2000, *ApJ*, 533, 682
- Cardamone, C., Schawinski, K., Sarzi, M., et al. 2009, *MNRAS*, 399, 1191
- Cardelli, J. A., Clayton, G. C., & Mathis, J. S. 1989, *ApJ*, 345, 245
- Cayrel, R. 1988, in *The Impact of Very High S/N Spectroscopy on Stellar Physics*, ed. G. Cayrel de Strobel & M. Spite, Vol. 132, 345
- Chabrier, G. 2003, *PASP*, 115, 763
- Chambers, K. C., Magnier, E. A., Metcalfe, N., et al. 2016a, arXiv e-prints, arXiv:1612.05560
- Chambers, K. C., Magnier, E. A., Metcalfe, N., et al. 2016b, arXiv e-prints, arXiv:1612.05560
- Chandra, P., Chevalier, R. A., Chugai, N., Fransson, C., & Soderberg, A. M. 2015, *ApJ*, 810, 32
- Chatzopoulos, E., Wheeler, J. C., & Vinko, J. 2012, *ApJ*, 746, 121
- Chen, T. W., Inserra, C., Fraser, M., et al. 2018, *ApJ*, 867, L31
- Chevalier, R. A. 2012, *ApJ*, 752, L2
- Chevalier, R. A. & Fransson, C. 2003, in *Supernovae and Gamma-Ray Bursters*, ed. K. Weiler, Vol. 598 (Springer), 171–194
- Chugai, N. N. 2019, *Astronomy Letters*, 45, 71
- Chugai, N. N., Blinnikov, S. I., Cumming, R. J., et al. 2004, *MNRAS*, 352, 1213
- Conroy, C., Gunn, J. E., & White, M. 2009, *ApJ*, 699, 486
- Coughlin, M. W., Bloom, J. S., Nir, G., et al. 2023, *ApJS*, 267, 31
- Crowther, P. 2012, *Astronomy and Geophysics*, 53, 4.30
- Crowther, P. A. 2007, *ARA&A*, 45, 177
- Davidson, K. & Humphreys, R. M. 2012, *Nature*, 486, E1
- De, K., Eilers, C., & Simcoe, R. 2022, *Transient Name Server AstroNote*, 28, 1
- De, K., Hankins, M. J., Kasliwal, M. M., et al. 2020, *PASP*, 132, 025001
- Dekany, R., Smith, R. M., Riddle, R., et al. 2020, *PASP*, 132, 038001
- Dessart, L., Audit, E., & Hillier, D. J. 2015, *MNRAS*, 449, 4304
- Dey, A., Schlegel, D. J., Lang, D., et al. 2019, *AJ*, 157, 168
- Dopita, M. A., Kewley, L. J., Sutherland, R. S., & Nicholls, D. C. 2016, *Ap&SS*, 361, 61
- Dwarkadas, V. V. 2011, *MNRAS*, 412, 1639
- Dwarkadas, V. V. 2019, *IAU Symposium*, 346, 83
- Dwek, E., Sarangi, A., Arendt, R. G., et al. 2021, *ApJ*, 917, 84
- Ekström, S., Georgy, C., Eggenberger, P., et al. 2012, *A&A*, 537, A146
- Elbaz, D., Daddi, E., Le Borgne, D., et al. 2007, *A&A*, 468, 33
- Elmegreen, D. M., Elmegreen, B. G., Sánchez Almeida, J., et al. 2012, *ApJ*, 750, 95
- Evans, P. A., Beardmore, A. P., Page, K. L., et al. 2009, *MNRAS*, 397, 1177
- Evans, P. A., Beardmore, A. P., Page, K. L., et al. 2007, *A&A*, 469, 379
- Evans, P. A., Page, K. L., Osborne, J. P., et al. 2020, *ApJS*, 247, 54
- Foreman-Mackey, D., Sick, J., & Johnson, B. 2014, *Python-Fsps: Python Bindings To Fsps (V0.1.1)*
- Fox, O. D., Fransson, C., Smith, N., et al. 2020, *MNRAS*, 498, 517
- Fransson, C., Chevalier, R. A., Filippenko, A. V., et al. 2002, *ApJ*, 572, 350
- Fransson, C., Ergon, M., Challis, P. J., et al. 2014, *ApJ*, 797, 118
- Fraser, M. 2020, *Royal Society Open Science*, 7, 200467
- Fraser, M., Inserra, C., Jerkstrand, A., et al. 2013, *MNRAS*, 433, 1312
- Fremming, C. 2021, *Transient Name Server Discovery Report*, 2021-3820, 1
- Fuller, J. 2017, *MNRAS*, 470, 1642
- Gal-Yam, A. 2012, *Science*, 337, 927
- Gal-Yam, A. 2019, *ARA&A*, 57, 305
- Gal-Yam, A., Leonard, D. C., Fox, D. B., et al. 2007, *ApJ*, 656, 372
- Goldoni, P., Royer, F., François, P., et al. 2006, in *Society of Photo-Optical Instrumentation Engineers (SPIE) Conference Series*, Vol. 6269, Society of Photo-Optical Instrumentation Engineers (SPIE) Conference Series, ed. I. S. McLean & M. Iye, 62692K
- Graham, M. J., Kulkarni, S. R., Bellm, E. C., et al. 2019, *PASP*, 131, 078001
- Groh, J. H. 2017, *Philosophical Transactions of the Royal Society of London Series A*, 375, 20170219
- Groh, J. H., Meynet, G., & Ekström, S. 2013, *A&A*, 550, L7
- Gröningsson, P., Fransson, C., Lundqvist, P., et al. 2006, *A&A*, 456, 581
- Gutiérrez, C. P., Anderson, J. P., Hamuy, M., et al. 2017, *ApJ*, 850, 89
- Habergham, S. M., Anderson, J. P., James, P. A., & Lyman, J. D. 2014, *MNRAS*, 441, 2230
- Haser, S. M., Pauldrach, A. W. A., Lennon, D. J., et al. 1998, *A&A*, 330, 285
- Heger, A., Fryer, C. L., Woosley, S. E., Langer, N., & Hartmann, D. H. 2003, *ApJ*, 591, 288
- Henry, A., Berg, D. A., Scarlata, C., Verhamme, A., & Erb, D. 2018, *ApJ*, 855, 96
- HI4PI Collaboration, Ben Bekhti, N., Flöer, L., et al. 2016, *A&A*, 594, A116
- Hoffman, J. L., Leonard, D. C., Chornock, R., et al. 2008, *ApJ*, 688, 1186
- Huang, C. & Chevalier, R. A. 2018, *MNRAS*, 475, 1261
- Humphreys, R. M. & Davidson, K. 1994, *PASP*, 106, 1025
- Israelian, G. & de Groot, M. 1999, *Space Sci. Rev.*, 90, 493
- Janka, H.-T. 2012, *Annual Review of Nuclear and Particle Science*, 62, 407
- Jeffery, D. J. 1999, arXiv e-prints, astro
- Jencson, J. E., Prieto, J. L., Kochanek, C. S., et al. 2016, *MNRAS*, 456, 2622
- Jerkstrand, A. 2017, in *Handbook of Supernovae*, ed. A. W. Alsabti & P. Murdin (Springer), 795
- Jerkstrand, A., Maeda, K., & Kawabata, K. S. 2020, *Science*, 367, 415
- Johnson, B. D., Leja, J., Conroy, C., & Speagle, J. S. 2021a, *ApJS*, 254, 22
- Johnson, B. D., Leja, J., Conroy, C., & Speagle, J. S. 2021b, *ApJS*, 254, 22
- Jordan, C. 1969, *MNRAS*, 142, 501
- Justham, S., Podsiadlowski, P., & Vink, J. S. 2014, *ApJ*, 796, 121

¹³ <https://wiserep.weizmann.ac.il/>

- Kankare, E., Ergon, M., Bufano, F., et al. 2012, *MNRAS*, 424, 855
- Kelly, P. L. & Kirshner, R. P. 2012, *ApJ*, 759, 107
- Kewley, L. J., Nicholls, D. C., & Sutherland, R. S. 2019, *ARA&A*, 57, 511
- Khatami, D. & Kasen, D. 2023, arXiv e-prints, arXiv:2304.03360
- Kim, Y. L., Rigault, M., Neill, J. D., et al. 2022, *PASP*, 134, 024505
- Komossa, S., Zhou, H., Rau, A., et al. 2009, *ApJ*, 701, 105
- Kurfürst, P. & Krůčka, J. 2019, *A&A*, 625, A24
- Lamers, H. J. G. L. M. 1989, in *Astrophysics and Space Science Library*, Vol. 157, IAU Colloq. 113: Physics of Luminous Blue Variables, ed. K. Davidson, A. F. J. Moffat, & H. J. G. L. M. Lamers, 135
- Lamperti, I., Koss, M., Trakhtenbrot, B., et al. 2017, *MNRAS*, 467, 540
- Lang, D. 2014, *AJ*, 147, 108
- Langer, N. 2012, *ARA&A*, 50, 107
- Leloudas, G., Schulze, S., Krühler, T., et al. 2015, *MNRAS*, 449, 917
- Liu, S., Luo, A. L., Yang, H., et al. 2022, *ApJ*, 927, 57
- Luridiana, V., Morisset, C., & Shaw, R. A. 2014, *Å*, 573, A42
- Mandigo-Stoba, M. S., Fremling, C., & Kasliwal, M. 2022, *The Journal of Open Source Software*, 7, 3612
- Martin, D. C., Fanson, J., Schiminovich, D., et al. 2005, *ApJ*, 619, L1
- Masci, F. J., Laher, R. R., Rusholme, B., et al. 2019, *PASP*, 131, 018003
- Mauerhan, J. & Smith, N. 2012, *MNRAS*, 424, 2659
- Modigliani, A., Goldoni, P., Royer, F., et al. 2010, in *Society of Photo-Optical Instrumentation Engineers (SPIE) Conference Series*, Vol. 7737, *Observatory Operations: Strategies, Processes, and Systems III*, ed. D. R. Silva, A. B. Peck, & B. T. Soifer, 773728
- Moriya, T. J. 2014, arXiv e-prints, arXiv:1402.2519
- Moriya, T. J., Galbany, L., Jimenez-Palau, C., et al. 2023, arXiv e-prints, arXiv:2306.09647
- Moriya, T. J., Maeda, K., Taddia, F., et al. 2014, *MNRAS*, 439, 2917
- Moriya, T. J., Sorokina, E. I., & Chevalier, R. A. 2018, *Space Sci. Rev.*, 214, 59
- Moriya, T. J., Stritzinger, M. D., Taddia, F., et al. 2020, *A&A*, 641, A148
- Munoz-Tunon, C., Sanchez Almeida, J., Elmegreen, D. M., & Elmegreen, B. G. 2014, arXiv e-prints, arXiv:1404.5170
- Nicholl, M. 2018, *Research Notes of the American Astronomical Society*, 2, 230
- Nicholl, M., Blanchard, P. K., Berger, E., et al. 2020, *Nature Astronomy*, 4, 893
- Nyholm, A., Sollerman, J., Tartaglia, L., et al. 2020, *A&A*, 637, A73
- Ofek, E. O., Sullivan, M., Shaviv, N. J., et al. 2014, *ApJ*, 789, 104
- Oke, J. B., Cohen, J. G., Carr, M., et al. 1995, *PASP*, 107, 375
- Oke, J. B. & Sargent, W. L. W. 1968, *ApJ*, 151, 807
- Orlitová, I., Verhamme, A., Henry, A., et al. 2018, *Astronomy & Astrophysics*, 616, A60
- Osterbrock, D. E. & Ferland, G. J. 2006, *Astrophysics of gaseous nebulae and active galactic nuclei* (Springer)
- Pastorello, A., Benetti, S., Brown, P. J., et al. 2015, *MNRAS*, 449, 1921
- Perley, D. A. 2019, *PASP*, 131, 084503
- Perley, D. A., Quimby, R. M., Yan, L., et al. 2016, *ApJ*, 830, 13
- Pettini, M. & Pagel, B. E. J. 2004, *MNRAS*, 348, L59
- Pozdnyakov, L. A., Sobol, I. M., & Syunyaev, R. A. 1983, *Astrophysics Space Physics Research*, 2, 189
- Prochaska, J. X., Hennawi, J., Cooke, R., et al. 2020a, *pypeit/PypeIt: Release 1.0.0*
- Prochaska, J. X., Hennawi, J. F., Westfall, K. B., et al. 2020b, arXiv e-prints, arXiv:2005.06505
- Prochaska, J. X., Hennawi, J. F., Westfall, K. B., et al. 2020, *Journal of Open Source Software*, 5, 2308
- Pursiainen, M., Leloudas, G., Paraskeva, E., et al. 2022, *A&A*, 666, A30
- Ransome, C. L., Habergham-Mawson, S. M., Darnley, M. J., et al. 2021, *MNRAS*, 506, 4715
- Ransome, C. L., Habergham-Mawson, S. M., Darnley, M. J., James, P. A., & Percival, S. M. 2022, *MNRAS*, 513, 3564
- Rigault, M., Neill, J. D., Blagorodnova, N., et al. 2019, *A&A*, 627, A115
- Roming, P. W. A., Pritchard, T. A., Prieto, J. L., et al. 2012, *ApJ*, 751, 92
- Rosado-Belza, D., Lisenfeld, U., Hibbard, J., et al. 2019, *A&A*, 623, A154
- Sana, H., de Mink, S. E., de Koter, A., et al. 2012, *Science*, 337, 444
- Schlegel, E. M. 1990, *MNRAS*, 244, 269
- Schulze, S., Krühler, T., Leloudas, G., et al. 2018, *MNRAS*, 473, 1258
- Schulze, S., Yaron, O., Sollerman, J., et al. 2021, *ApJS*, 255, 29
- Selsing, J., Malesani, D., Goldoni, P., et al. 2019, *A&A*, 623, A92
- Shingles, L., Smith, K. W., Young, D. R., et al. 2021, *Transient Name Server AstroNote*, 7, 1
- Silverman, J. M., Nugent, P. E., Gal-Yam, A., et al. 2013, *ApJ*, 772, 125
- Smartt, S. J. 2009, *ARA&A*, 47, 63
- Smith, K. W., Smartt, S. J., Young, D. R., et al. 2020, *PASP*, 132, 085002
- Smith, N. 2011, *MNRAS*, 415, 2020
- Smith, N. 2013, *MNRAS*, 429, 2366
- Smith, N. 2017a, in *Handbook of Supernovae*, ed. A. W. Alsabti & P. Murdin (Springer), 403
- Smith, N. 2017b, *Philosophical Transactions of the Royal Society of London Series A*, 375, 20160268
- Smith, N., Hinkle, K. H., & Ryde, N. 2009a, *AJ*, 137, 3558
- Smith, N., Li, W., Miller, A. A., et al. 2011, *ApJ*, 732, 63
- Smith, N., Silverman, J. M., Chornock, R., et al. 2009b, *ApJ*, 695, 1334
- Speagle, J. S. 2020, *MNRAS*, 493, 3132
- Spergel, D. N., Bean, R., Doré, O., et al. 2007, *ApJS*, 170, 377
- Stasińska, G. 1982, *A&AS*, 48, 299
- Stoll, R., Prieto, J. L., Stanek, K. Z., et al. 2011, *ApJ*, 730, 34
- Stritzinger, M., Taddia, F., Fransson, C., et al. 2012, *ApJ*, 756, 173
- Suzuki, A., Maeda, K., & Shigeyama, T. 2016, *ApJ*, 825, 92
- Suzuki, A., Moriya, T. J., & Takiwaki, T. 2019, *ApJ*, 887, 249
- Taddia, F., Stritzinger, M. D., Fransson, C., et al. 2020, *A&A*, 638, A92
- Taddia, F., Stritzinger, M. D., Sollerman, J., et al. 2013, *A&A*, 555, A10
- Tonry, J. L., Denneau, L., Heinze, A. N., et al. 2018, *PASP*, 130, 064505
- Trundle, C., Kotak, R., Vink, J. S., & Meikle, W. P. S. 2008, *A&A*, 483, L47
- Trundle, C., Pastorello, A., Benetti, S., et al. 2009, *A&A*, 504, 945
- Tsang, B. T. H., Kasen, D., & Bildsten, L. 2022, *ApJ*, 936, 28
- Turatto, M., Cappellaro, E., Danziger, I. J., et al. 1993, *MNRAS*, 262, 128
- van der Walt, S., Crellin-Quick, A., & Bloom, J. 2019, *The Journal of Open Source Software*, 4, 1247
- van Dokkum, P. G. 2001, *PASP*, 113, 1420
- Vernet, J., Dekker, H., D'Odorico, S., et al. 2011, *A&A*, 536, A105
- Vink, J. S. 2008, *New A Rev.*, 52, 419
- Vink, J. S., de Koter, A., & Kotak, R. 2008, in *Astronomical Society of the Pacific Conference Series*, Vol. 388, *Mass Loss from Stars and the Evolution of Stellar Clusters*, ed. A. de Koter, L. J. Smith, & L. B. F. M. Waters, 47
- Weis, K. 2001, *Reviews in Modern Astronomy*, 14, 261
- Weis, K. & Bomans, D. J. 2020, *Galaxies*, 8, 20
- Wood-Vasey, W. M., Wang, L., & Aldering, G. 2004, *ApJ*, 616, 339
- Woosley, S. E. 2017, *ApJ*, 836, 244
- Woosley, S. E. 2018, *ApJ*, 863, 105
- Woosley, S. E. & Weaver, T. A. 1995, *ApJS*, 101, 181
- Wright, A. H., Robotham, A. S. G., Bourne, N., et al. 2016, *MNRAS*, 460, 765
- Wright, E. L., Eisenhardt, P. R. M., Mainzer, A. K., et al. 2010, *AJ*, 140, 1868
- Yan, L., Quimby, R., Ofek, E., et al. 2015, *ApJ*, 814, 108
- Yang, H., Malhotra, S., Gronke, M., et al. 2016, *The Astrophysical Journal*, 820, 130
- Yaron, O. & Gal-Yam, A. 2012, *PASP*, 124, 668
- Zapartas, E., de Mink, S. E., Justham, S., et al. 2019, *A&A*, 631, A5
- Zhang, T., Wang, X., Wu, C., et al. 2012, *AJ*, 144, 131